

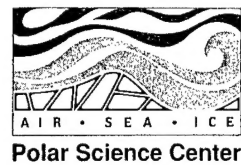
REPORT DOCUMENTATION PAGE				<i>Form Approved OMB No. 0704-0188</i>	
<p>Public reporting burden for this collection of information is estimated to average 1 hour per response, including the time for reviewing instructions, searching data sources, gathering and maintaining the data needed, and completing and reviewing the collection of information. Send comments regarding the burden estimate or any other aspect of this collection of information, including suggestions for reducing this burden to Washington Headquarters Service, Directorate for Information Operations and Reports, 1215 Jefferson Davis Highway, Suite 1204, Arlington, VA 22202-4302, and to the Office of Management and Budget, Paperwork Reduction Project (0704-0188) Washington, DC 20503.</p> <p>PLEASE DO NOT RETURN YOUR FORM TO THE ABOVE ADDRESS.</p>					
1. REPORT DATE (DD-MM-YYYY) 6/10/03		2. REPORT DATE FINAL		3. DATES COVERED (From - To) 1/1/96-12/31/02	
4. TITLE AND SUBTITLE Testing of the Autonomous Microconductivity-Temperature Vehicle and a Direct Technique for the Determination of Turbulent Fluxes with Autonomous Underwater Vehicles		5a. CONTRACT NUMBER 5b. GRANT NUMBER N00014-96-1-5033 5c. PROGRAM ELEMENT NUMBER 5d. PROJECT NUMBER 5e. TASK NUMBER 5f. WORK UNIT NUMBER			
6. AUTHOR(S) James H. Morison		5d. PROJECT NUMBER 5e. TASK NUMBER 5f. WORK UNIT NUMBER			
7. PERFORMING ORGANIZATION NAME(S) AND ADDRESS(ES) Polar Science Center, Applied Physics Laboratory University of Washington 1013 NE 40th Street Seattle, WA 98105-6698		8. PERFORMING ORGANIZATION REPORT NUMBER			
9. SPONSORING/MONITORING AGENCY NAME(S) AND ADDRESS(ES) Office of Naval Research, Team Leader Thomas B. Curtin Ballston Centre Tower One 800 North Quincy Street, Arlington, VA 22217-5660		10. SPONSOR/MONITOR'S ACRONYM(S) ONR 11. SPONSORING/MONITORING AGENCY REPORT NUMBER			
12. DISTRIBUTION AVAILABILITY STATEMENT distribution is unlimited					
13. SUPPLEMENTARY NOTES					
14. ABSTRACT The objectives of ONR grant N00014-96-1-5033, "Testing of the Autonomous Microconductivity-Temperature Vehicle and a Direct Technique for the Determination of Turbulent Fluxes with Autonomous Underwater Vehicles," were to develop a technique to measure vertical water velocity and the turbulent fluxes of heat and salt with autonomous underwater vehicles, and to test the technique by using a new vehicle to measure variability in the upper ocean around summer at the Surface Heat Balance of the Arctic (SHEBA) station. In the last three years the grant has exclusively covered support for our graduate student, Dan Hayes, to perfect the Kalman smoothing technique, analyze the SHEBA data, and develop a model to explain the observations.					
15. SUBJECT TERMS arctic, autonomous underwater vehicle, high latitude dynamics, turbulent fluxes, Kalman smoothing method					
16. SECURITY CLASSIFICATION OF: a. REPORT b. ABSTRACT c. THIS PAGE			17. LIMITATION OF ABSTRACT	18. NUMBER OF PAGES	19a. NAME OF RESPONSIBLE PERSON James H. Morison 19b. TELEPHONE NUMBER (Include area code) 206-543-1394
U	U	U	UU	3	

Standard Form 298 (Rev. 8-98)
Prescribed by ANSI-Std Z39-18

BEST AVAILABLE COPY



Applied Physics Laboratory
College of Ocean and Fishery Sciences, University of Washington



9 June 2003

Dr. Thomas B. Curtin
Team Leader Ocean Modeling and Prediction
Office of Naval Research
800 North Quincy Street
Arlington, VA 22217-5660

Subj: Final Report, ONR Grant N00014-96-1-5033

Dear Tom,

The objectives of ONR grant N00014-96-1-5033, "Testing of the Autonomous Microconductivity-Temperature Vehicle and a Direct Technique for the Determination of Turbulent Fluxes with Autonomous Underwater Vehicles," were to develop a technique to measure vertical water velocity and the turbulent fluxes of heat and salt with autonomous underwater vehicles, and to test the technique by using a new vehicle to measure variability in the upper ocean around summer at the Surface Heat Balance of the Arctic (SHEBA) station. In the last three years the grant has exclusively covered support for our graduate student, Dan Hayes, to perfect the Kalman smoothing technique, analyze the SHEBA data, and develop a model to explain the observations. I have supervised Dan in this project with the support of ONR grant N00014-98-1-0037, Arctic Mixed Layer Dynamics.

Dan has completed development of the Kalman smoothing method. The accuracy has been improved, and the frequency response of the velocity estimates has been extended by accounting for the vehicle pitching moment caused by the variation in vertical water velocity along the length of the hull. This was done by approximating the effect of differences in vertical velocity along the vehicle hull with an additional first order lag response in the vehicle equation of state. The Kalman smoother method now produces turbulent vertical velocity spectra from the AMTV that agree with spectra from fixed velocity sensors up to wave numbers of 0.5 cpm or wavelengths of 2 meters. This is nearly the theoretical limit associated with the 1.6-meter vehicle hull length. A paper on this work was published in *The Journal of Atmospheric and Oceanic Technology*, [Hayes and Morison, 2002].

Most of our efforts have focused on explaining results obtained under and around a large lead on August 7, 1998 during a storm. The data from this period is central to one of the key questions of the SHEBA oceanography program, the effects of horizontal variability on the boundary layer. High downward heat flux measured in the lead agrees with fixed sensor measurements at the lead edge and corresponds roughly to the input of radiative heat at the lead surface. Heat flux at 5 m depth remains elevated downstream under the ice, because the internal boundary layer associated with drastically reduced heat input, takes 100 m to grow to a depth of 5 m. The salt flux follows a similar pattern supplied by the flux of fresh melt water accumulated

near the lead surface from the surrounding ice. The turbulent velocity fluctuations increase under the ice and increase in length scale beyond 100 m of the lead edge, probably due to a combination of the rough ice surface and absence of stabilizing buoyancy flux under the ice. These observations have lead us to speculate that unstable stratification may occur, even under nominally stabilizing buoyancy flux, by the interaction of vertical shear and horizontally inhomogeneous salinity. McPhee (personal communication) has suggested such an "overrunning" phenomena, whereby velocity shear drags dense water over an adjacent fresh water patch, as a possible reason for observed rates of mixing at SHEBA that occasionally were greater than would be predicted.

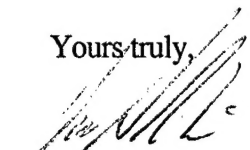
To understand the summer lead phenomena observed with the AMTV, Hayes first simulated steady, two-dimensional (x and z), forced convection using a simple advective transformation ($x=V_{ice} t$) from Mellor *et al.* [1986]. This converts the problem to a one-dimensional (z) time-dependent problem. The method accounts for spatial variability due to growing boundary layers, but because it is not truly two-dimensional, it does not take into account the effects of horizontal pressure variation or allow for the propagation of horizontally inhomogeneous initial conditions. The one-dimensional, time-dependent model is based on one by McPhee (personal communication) and uses the McPhee [1994] turbulent closure method.

The simulated temperature and salinity changes under and beyond the lead are similar to measured changes except that the simulated 5-m temperature begins to decrease immediately at the edge. Only at slightly deeper depths does the simulated temperature continue to increase for a few hundred meters downstream before leveling off. The measured temperature continues to increase for 100 m downstream of the lead edge. The simulated heat fluxes in the lead are comparable to the measurements. They remain large downward farther downstream than the measured fluxes. The simulations show that the heat put into the lead continues to be mixed downward into the mixed layer for a considerable distance downstream of the lead. The simulated turbulent velocity scale and mixing length are consistent with the appearance of the measured w' , energy and mixing length increase under the ice.

The boundary layer adjustment model explains many of the observed characteristics of summer lead flux for steady conditions. However, it is inherently incapable of simulating the overrunning phenomena associated with shear flow in the presence of horizontal variability. For this the evolution of the shear flow must be simulated in the presence of an existing horizontal gradient in salinity. For this a true time-varying 2 or 3-D model is required. To develop such a model Dan has modified a 3-D non-hydrostatic model provided by David Smith at Arizona State University. The code has been streamlined, and adapted to the summer lead problem. Doubly-periodic horizontal boundary conditions were implemented. A surface stress boundary condition has been added, and mean velocity profiles have been simulated as a neutrally stratified test case. Dan's supervisory committee (Miles McPhee, James Morison, Peter Rhines, Mark Warner, John Wetzlaufer) has recommended that he not attempt to simulate the problem with a large-eddy simulation, but rather that he simplify the problem with a turbulent closure approach. With the simple model, he will investigate the flow regimes with horizontally inhomogeneous initial conditions and for various values of surface buoyancy flux, fresh water patch size, flow velocity, and eddy viscosity. SHEBA observations will provide bounds for these parameters. Complexity is being added to the model in steps through mean background velocity, eddy viscosity, and ice topography. The comparison of model results with AMTV and ROV data will improve our understanding horizontally inhomogeneous stably-stratified boundary layers generally and the flux distribution measured during various periods at SHEBA specifically.

Dan passed his General Exam in late May 2000. His committee approved his Ph.D. thesis proposal to use the SHEBA AMTV results in conjunction with boundary layer modeling to understand the effect of horizontal variability in stably stratified boundary layers. Dan successfully defended his thesis on June 9, 2003.

Thank you for your support of this research.

Yours truly,

James Morison

References

Hayes, D. and J. Morison, 2002, Determining Turbulent, Vertical Fluxes of Heat and Salt in the Polar Ocean Boundary Layer with an Autonomous Underwater Vehicle, *Journal of Atmospheric and Oceanic Technology*, 19, 759-779..

McPhee, M. G., 1994, On the turbulent mixing length in the oceanic boundary layer, *J. Phys Oceanogr.*, 24, 2014-2031.

Mellor, G. L, M. G. McPhee, and M. Steele, 1986, Ice-seawater turbulent boundary layer interaction with melting or freezing, *J. Phys. Oceanogr.*, 16(11), 1829-1846.

Attachment: Hayes and Morison, 2002

Cc: ONR Seattle
 DTIC w/SF298
 NRL w/SF298

Determining Turbulent Vertical Velocity, and Fluxes of Heat and Salt with an Autonomous Underwater Vehicle

DANIEL R. HAYES AND JAMES H. MORISON

Polar Science Center, Applied Physics Laboratory, University of Washington, Seattle, Washington

(Manuscript received 10 October 2000, in final form 6 September 2001)

ABSTRACT

The authors show that vertical turbulent fluxes in the upper ocean can be measured directly with an autonomous underwater vehicle (AUV). A horizontal profile of vertical water velocity is obtained by applying a Kalman smoother to AUV motion data. The smoother uses a linearized model for vehicle motion and vehicle data such as depth, pitch, and pitch rate to produce an optimal estimate of the state of the system, which includes other vehicle variables and the vertical water velocity. Vertical water velocity estimated by applying the smoother to data from the autonomous microconductivity temperature vehicle (AMTV) is accurate at horizontal scales from three to several hundred meters, encompassing the energy-containing scales of most oceanic turbulence. The zero-lag covariances between vertical water velocity and concurrent measurements of temperature or salinity represent the heat and salt fluxes, respectively. The authors have measured horizontal profiles of turbulent fluxes with two different AUVs in three separate polar ocean experiments using this technique. Flux magnitudes and directions are reasonable and in general agreement with fixed turbulence sensors. With this technique, one can gather boundary layer data in inaccessible regions without disturbing or affecting the surface.

1. Introduction

The vertical turbulent fluxes of heat and salt in the oceanic boundary layer are critical elements of ocean-sea-ice-atmosphere interaction. The fluxes are defined in the Reynolds decomposition of the heat and salt conservation equations as $F_{\text{heat}} = \rho C_p \langle w_w T' \rangle$, and $F_{\text{salt}} = \rho \langle w_w S' \rangle$, where w_w is the turbulent fluctuation in vertical water velocity, T' and S' are the fluctuations in temperature and salinity (in parts per thousand) from their respective means, ρ is the mean water density, and C_p is the specific heat capacity of the water. The angle brackets indicate an ensemble average over many realizations of the turbulent flow. These fluxes are difficult to measure directly primarily because it is difficult to measure w_w , especially in the open ocean where a stable measurement platform is nearly impossible to achieve. A variety of indirect methods (e.g., Osborn and Cox 1972) have been developed to estimate the fluxes based on measurements at the smallest scales of turbulence and the assumption of a steady-state energy cascade from the energy-containing turbulence scales to the dissipation scales. In general, indirect methods assume steady and homogeneous turbulence. See Fleury and Lueck (1994) for a review of indirect methods.

Direct measurements of the turbulent fluxes have been

made in polar seas where the ice cover provides a stable platform from which sensitive velocity sensors can be suspended. McPhee (1994) and McPhee and Stanton (1996) describe under-ice deployment of vertical masts of turbulence instrument clusters (TICs) composed of orthogonal velocity, temperature, and conductivity sensors. McPhee and Stanton (1996) also compare direct flux measurements to fluxes estimated using a turbulent microstructure profiler and assuming a local balance between production and dissipation of turbulent kinetic energy.

However, observations in the under-ice boundary layer present their own special challenges. Chief among these is the spatial variability of the under-ice boundary layer. The ice cover may consist of large areas of thick multiyear ice, smooth new ice, and open water. Each type of surface provides a different surface boundary condition with unique fluxes of heat, salt, and momentum. The effect of this horizontal variability has become a primary area of interest in the study of air-sea-ice-ocean interaction. Notable recent efforts in this area have been the 1992 Lead Experiment (LeadEx Group 1993) and several projects as part of the 1997-98 Surface Heat Balance of the Arctic Ocean (SHEBA) program. However, in these situations the fixed sensor method of measuring boundary layer conditions is limited because it does not resolve horizontal variability, and it cannot be used under some types of surfaces [e.g., thin ice and open water]. In order to overcome these difficulties Morison and McPhee (1998, hereafter

Corresponding author address: James H. Morison, Applied Physics Laboratory, 1013 NE 40th St., Seattle, WA 98105.
E-mail: morison@apl.washington.edu

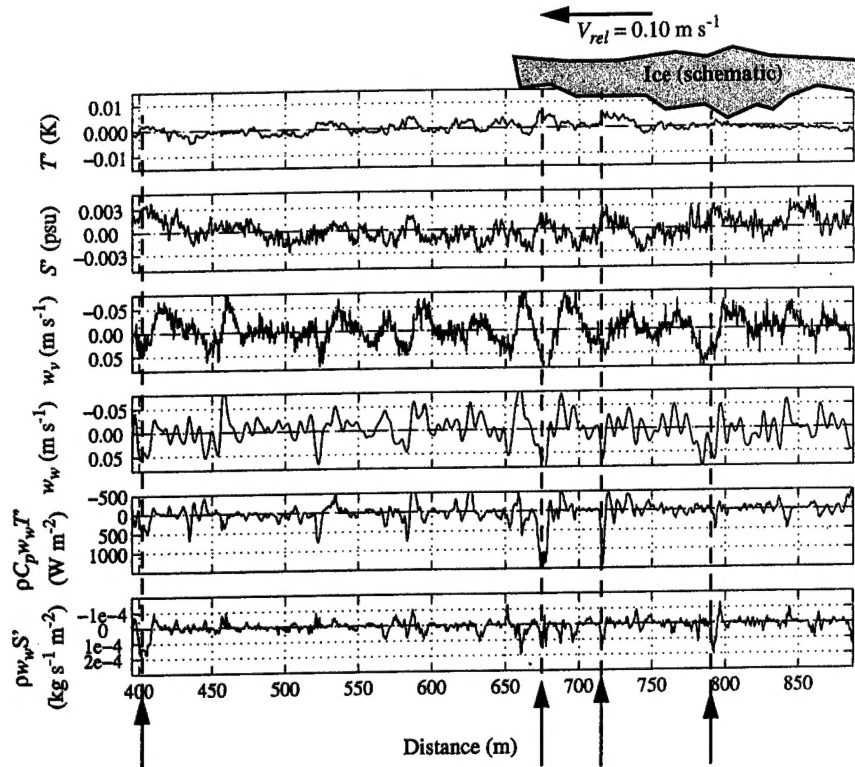


FIG. 1. ACTV data from lead 3, run 4, leg 3 of LeadEx. Mean vehicle depth was 15 m, speed was 1.65 m s^{-1} , and the mean ice-ocean relative velocity was 0.10 m s^{-1} . The data have been smoothed with a 1-m bin average, except for differentiated vehicle depth (w_v), which has been smoothed by a 5-m bin. Vertical water velocity, w_w , is estimated using a Kalman smoother on vehicle depth. See text. Several warm, salty downcurrents are indicated. The mean heat flux is 54 W m^{-2} , and the mean salt flux is $1.1 \times 10^{-5} \text{ kg s}^{-1} \text{ m}^{-2}$, positive downward. Correlation coefficients between vertical water velocity and temperature and velocity and salinity are significant at 0.23 for both.

MM98) combined measurements from the autonomous conductivity temperature vehicle (ACTV) and TICs to examine unstable haline convection from winter leads during LeadEx. The ACTV is a small, near-neutrally buoyant autonomous underwater vehicle (AUV) that travels a programmed course beneath leads and sea ice. It measures temperature and salinity with an onboard conductivity-temperature-depth (CTD) meter. MM98 found that the small rates of change of ACTV depth during a programmed level cruise appeared to be correlated with fluctuations in salinity. This is illustrated in Fig. 1 showing a sample of data from the ACTV taken during LeadEx. The panel labeled w_v is the vertical velocity of the ACTV inferred from vehicle depth. Many of the downward peaks in w are correlated with positive peaks in the salinity variation, S' . This suggests the vehicle moves downward with the saline, convective plumes. The vehicle acts roughly like a Lagrangian drifter with respect to small vertical motions, even while it moves horizontally at 1.7 m s^{-1} . Such observations led to the idea that vehicle motion could be used to estimate vertical water velocity. An ad hoc low-pass filter was used by MM98 to improve the agreement between the

ACTV-derived vertical velocity and the vertical velocity spectra measured by the fixed TIC. The resulting ACTV velocity estimates were combined with the vehicle temperature and salinity measurements to directly derive horizontal profiles of the instantaneous local salt and heat fluxes, $w_w S'$ and $w_w T'$. Suitable profile averages of these agreed with estimates of fluxes made by other means and revealed among other things strong convective activity at the lead edges.

Other researchers have measured turbulent quantities with horizontally profiling instruments. Fleury and Lueck (1994) have used a shear probe on a towed vehicle to directly calculate heat and buoyancy flux on scales of 0.25 – 1 m. They noted that larger-scale motions that may have contributed significantly to the fluxes were contaminated by body motions. Levine and Lueck (1999) have used a shear probe on an AUV to estimate the rate of dissipation of kinetic energy along a horizontal track. Submarines have also been used by Yamazaki and Osborn (1993) to gather horizontal profiles of turbulent quantities using a shear probe. They calculated turbulent fluxes directly to validate eddy diffusivity models used by indirect techniques of estimat-

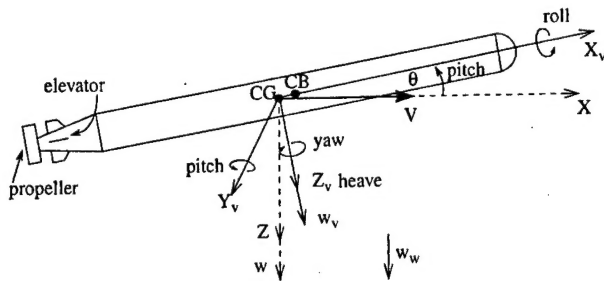


FIG. 2. ACTV schematic and both vehicle-centered and earth-centered (inertial) reference frames. The Y_v axis extends out of the page, and downward is positive in both frames. The velocity, V , is assumed known and constant. The center of gravity (CG) and center of buoyancy (CB) are indicated.

ing heat flux. However none of these efforts, besides MM98, have attempted to make direct measurement of the turbulent fluxes in the boundary layer.

The MM98 method of estimating turbulent velocity and fluxes with the ACTV data produced solid results, but it is limited. An AUV has its own dynamic response to variable vertical water velocity, especially since it has a control system that returns it to a programmed run depth. In MM98 this is accounted for partially by the ad hoc filter. However, this method is not founded on a knowledge of the AUV's dynamics. Different AUVs will behave differently in a turbulent velocity field. Thus, the ad hoc filter method is not a general solution that could be applied in other areas with confidence without TIC measurements for comparison. Here we will describe a Kalman smoothing method for deriving vertical water velocity from the motion of an AUV. The Kalman smoothing technique uses a model of vehicle dynamics to make optimum estimates of vertical water velocity from measurements of vehicle motion. It will also be shown that these velocity estimates can be used to directly compute horizontal profiles of $w_w S'$ and $w_w T'$.

Section 2 describes two AUVs and their dynamic models, the estimation technique, and the technique's performance. The technique is illustrated in section 3 by calculating turbulent fluxes of heat and salt for both Arctic and Antarctic case studies and comparing AUV and fixed turbulence mast data. Section 4 presents a brief summary. Details on vehicle models and the Kalman smoother are left to the appendixes.

2. Methods

a. Instrumentation

The Kalman smoothing method has been applied to two AUVs, the ACTV and the more sophisticated autonomous microconductivity temperature vehicle (AMTV). A schematic of the ACTV is shown in Fig. 2. The vehicle is about 1.6 m long and 9 cm in diameter, with a mass of 9.6 kg. It travels a preprogrammed, dead-reckoned course at about 1.7 m s^{-1} , measuring temperature, conductivity,

and pressure. Horizontal position is recorded with an acoustic tracking system. The ACTV is described more fully by MM98. In MM98, TIC measurements of vertical water velocity are compared to the vertical velocity of the ACTV under the lead. This comparison relies on the assumption that the turbulent features may be treated as if they are frozen into the mean field and drift past the TIC at the mean flow speed (Taylor's hypothesis). This allows the time series observations of the TIC to be converted to spatial observations comparable to those made by the AUV. Spectra of TIC temperature and salinity converted to the spatial dimension in this way agree very well with the ACTV observations, confirming the applicability of Taylor's hypothesis. This method of comparison will be used here to validate the Kalman smoothing results. Samples of ACTV data from the LeadEx experiment and the 1994 Antarctic Zone Flux Experiment (ANZFLUX) experiment will be used to illustrate the Kalman smoother method.

A second vehicle, the AMTV, has been developed to take greater advantage of the Kalman smoothing scheme. It is based on the remotely operated underwater measurement system (REMUS) vehicle developed at the Woods Hole Oceanographic Institution. To more accurately estimate vehicle motion, the AMTV carries a precision Paroscientific pressure sensor and a Systron Donner Motion Pack package of accelerometers and sensitive pitch, roll, and yaw rate sensors. Of the motion pack sensors, we only use output of the forward accelerometer and pitch rate sensor in the Kalman smoother calculations. Of course the accelerometer signal is due to both acceleration of the vehicle and the effect of gravity at the pitch angle of the vehicle. For the range of vehicle motions studied here the acceleration component of the signal is less than 1% of the gravity-induced pitch angle signal. Therefore the accelerometer output is taken as a measure of pitch angle.

The AMTV employs fast-response Sea-Bird Electronics, SBE 7-02 microconductivity and SBE 7-01 microtemperature probes, as well as an upward-looking Tritech precision acoustic altimeter to measure ice draft. The AMTV is 1.6 m in length, 19 cm in diameter, and displaces 33 kg (Fig. 3). Pairs of elevator planes and rudder planes at the tail control its motion. It operates at speeds from 1.0 to 1.6 m s^{-1} under program control. Like the ACTV, a three-dimensional course is programmed into the AMTV. This may be a combination of dead-reckoning, acoustic navigation, and homing to one of two Benthos acoustic transponders. The two-dimensional position of the AMTV is displayed and recorded by 100-m baseline portable acoustic tracking range developed at the Applied Physics Laboratory (APL). The AMTV has the capability to home in on acoustic beacons, either to reach a desired checkpoint during a run, or to be recovered in a submerged panel of netting. AMTV data from the SHEBA summer lead experiment will be used to illustrate the performance of the Kalman

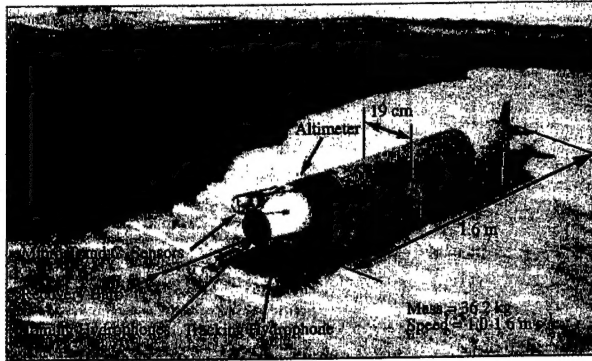


FIG. 3. The AMTV at SHEBA experiment site, Aug 1998. Specifications and vehicle components are indicated in the figure.

smoother for a vehicle in a unique setting incorporating more motion sensors.

b. Kalman smoothing

The Kalman smoother makes an estimate of system state that is an optimum combination of a dynamic model-based extrapolation and noisy measurements of a few components of the state (Gelb 1974). The smoother is founded on a linear state-space representation of the dynamic system being studied. That is, the system evolution is determined by multiple first-order differential equations for the rate of change of a vector of state variables. In our case, the position and velocity of an AUV at one time, along with the equations of motion allow us to predict its position and velocity at any later time. The motion of the vehicle is predicted from the sum of the forces acting on it, including buoyancy, the action of water flowing by it vertically, and forces exerted by the control surfaces. Because forces on the vehicle and measurements have random parts, the system model must include a random forcing function for vertical water velocity and an estimate of sensor noise to completely specify the system. The smoother uses the vehicle model and noisy observations to produce an optimal estimate of the true, unobservable state of the system. In other words, the smoother will estimate the portion of the system variability due to unforced motion of the body and due to noise. The vehicle forcing (vertical water velocity) is calculated to account for what remains of the measured variability.

In application, the Kalman smoother consists of two recursive filters that are run forward and backward over the vehicle data. Thus a smoother may only be applied after all data have been collected. For the sake of clarity and concreteness the simpler forward Kalman filter is presented here. The smoother is developed from the filter paradigm in appendix A. The filter is based on a system model (1), a measurement model (2), and initial conditions for the state vector (3):

$$\frac{d}{dt}\mathbf{x} = \mathbf{F}\mathbf{x} + \mathbf{G}\mathbf{v} \quad \mathbf{v} \sim \text{Normal}(0, \mathbf{Q}) \quad (1)$$

$$\mathbf{z} = \mathbf{H}\mathbf{x} + \mathbf{n} \quad \mathbf{n} \sim \text{Normal}(0, \mathbf{R}) \quad (2)$$

$$\mathbf{x} = \begin{bmatrix} w_w \\ w \\ q \\ z \\ \theta \end{bmatrix} = \begin{bmatrix} \text{vertical water velocity} \\ \text{vertical vehicle velocity} \\ \text{pitch rate} \\ \text{vehicle depth} \\ \text{vehicle pitch} \end{bmatrix}. \quad (3)$$

The system model is a first-order matrix differential equation for the vector of state variables, \mathbf{x} . The variables w , q , z , and θ are vehicle variables related to each other by the equations of vertical and pitching motion. The vertical water velocity, w_w , is inserted into the system model, so that it can be estimated directly by the Kalman technique. The first term on the right of (1) represents the system dynamics. Deterministic control inputs, which in our case are functions of the state vector, are subsumed into the dynamics term. The second term is the stochastic function representing the system forcing, which is assumed to be distributed normally with mean zero and noise covariance matrix \mathbf{Q} . The measurement vector, \mathbf{z} , is modeled in (2) as a combination of the true-state variables plus a normally distributed noise vector with zero mean and covariance matrix \mathbf{R} . In general, \mathbf{F} , \mathbf{G} , and \mathbf{H} may be functions of time, but here they are constant. All vectors have zero mean.

The forward Kalman filter seeks an estimate of the state vector just after the measurement as an optimum linear combination of the state vector just before the measurement and the measurement vector itself. The unknown coefficient matrices for the linear combination are found by requiring that the error in the estimate is unbiased, then forming the matrix of error covariances and minimizing the trace of this matrix. See Gelb (1974, chapter 4) for a complete derivation. The filter consists of the following system of equations describing the evolution of the state estimate, \mathbf{x}_f , and the error covariance, \mathbf{P}_f (Gelb 1974, p. 123). Subscripts indicate an estimate (forward in this case), and true but unknown values of \mathbf{x} have no subscripts:

$$\begin{aligned} \frac{d\mathbf{x}_f}{dt} &= \mathbf{F}\mathbf{x}_f + \mathbf{P}_f \mathbf{H}^T \mathbf{R}^{-1} [\mathbf{z} - \mathbf{H}\mathbf{x}_f] \\ \mathbf{x}_f(t = 0) &= \mathbf{x}_0 \end{aligned} \quad (4)$$

$$\begin{aligned} \frac{d\mathbf{P}_f}{dt} &= \mathbf{F}\mathbf{P}_f + \mathbf{P}_f \mathbf{F}^T + \mathbf{G}\mathbf{Q}\mathbf{G}^T - \mathbf{P}_f \mathbf{H}^T \mathbf{R}^{-1} \mathbf{H}\mathbf{P}_f \\ \mathbf{P}_f(t = 0) &= \mathbf{P}_0, \end{aligned} \quad (5)$$

where $\mathbf{P}_f = E[(\mathbf{x}_f - \mathbf{x})(\mathbf{x}_f - \mathbf{x})^T]$.

It is assumed that the random forcing, \mathbf{v} , and measurement noise, \mathbf{n} , are uncorrelated and that \mathbf{R}^{-1} exists (nonzero measurement noise). Given a vector of measurements, \mathbf{z} , the initial value problem can easily be

solved numerically for \mathbf{x} and \mathbf{P} using a prepackaged ordinary differential equation (ODE) solver. The appendix A linear filter is the optimum filter if both system and measurement noise are truly Gaussian. If they are not, the filter is only the optimum *linear* filter (Gelb 1974, p. 107). Intuitively, the forward estimate obeys the deterministic model, \mathbf{F} , when the measurement errors (\mathbf{R}) are large compared to the difference between the estimated and measured state, that is, the measurements are of little value to the estimate. The vertical water velocity estimate is simply the first element of the state estimate.

A considerable portion of effort in deriving a Kalman filter is in deriving the system model \mathbf{F} . This is discussed in detail for our vehicles in appendix B, but a brief summary is given here.

c. Linearized model for autonomous underwater vehicles

Bartlett and Schlachter (1967) and Nahon (1996) derive the complete set of equations of motion for torpedo-shaped bodies. These are for vehicle motion in still water. Here a simplified model is used for small vehicle motions in the vertical plane due to the action of vertical water velocity variations. The model is a linearized, two-dimensional system of equations. The vertical and angular motions (heave and pitch) of an underwater vehicle are best expressed in a body-centered reference frame, with the vehicle center of gravity as the origin (Etkin 1972). The oceanic boundary layer dynamics are naturally described in an earth-centered coordinate system. The vehicle- and earth-centered coordinate systems are illustrated in Fig. 2. In our initial derivations the water velocity is assumed constant over the length of the vehicle. (In a final refinement we modify this assumption.) The vehicle control system is assumed to be active, but it only attempts to constrain the vehicle to a constant run depth. The pitch (θ) and elevator deflection (δp) angles are assumed small. The equations in the vehicle-centered frame are further simplified by assuming the roll angle, roll rate, and yaw rate are zero. Vehicle horizontal velocity is assumed constant. Vehicle run data during straight and level flight analyzed here support these assumptions. The simplified equations of motion for vertical vehicle velocity (w_v) and pitch rate (q), are

$$m_T \dot{w}_v = Z_{w_v} w_{vrel} + (Z_q + m_L V) q + Z_{dp} \delta p + (mg - B) \quad (6)$$

$$J_y \dot{q} = M_{w_v} w_{vrel} + M_q q + M_{dp} \delta p + BX_{CB}. \quad (7)$$

In Eq. (6), w_v is the vertical acceleration of the AUV in the vehicle-centered coordinate system, w_{vrel} is the velocity of the AUV relative to the water in the

vehicle-coordinate system, q and \dot{q} are the pitch rate and pitch angular acceleration, and δp is the dive plane angle relative to the vehicle. The vehicle mass is m . The apparent longitudinal and transverse masses are represented by m_L and m_T , respectively. The apparent moment of inertia is J_y . The apparent mass (inertia) terms include the mass (inertia) plus the virtual mass (inertia) that arises because the fluid that surrounds an accelerating vehicle must also be accelerated. The body force of net buoyancy ($mg - B$) and the pitching moment due to a separation of the center of gravity and the center of buoyancy (BX_{CB}) are the constant terms in (6) and (7). One Coriolis term arises, $m_L V q$. All other nonconstant terms on the right-hand side are the hydrodynamic forces and moments arising from the motion of the vehicle relative to the water. These forces and moments are written as state variables multiplied by subscripted Z or M coefficients derived in appendix B. The force and moment coefficients are constant, since the vehicle travels at a constant speed, V . A complete list of symbol definitions is in appendix C.

Since both the depth and water velocity are referenced to true vertical, the equations of motion need to be expressed in the earth-centered reference frame. With vertical water velocity, w_w , defined positive downward and assumed uniform across the vehicle, referring to Fig. 2, and assuming the pitch angle, θ , is small, the following transformation expresses w_v and w_{vrel} in terms of the earth-centered vehicle vertical velocity, w , and water velocity, w_w :

$$w_v \approx w + V\theta \quad \text{and}$$

$$w_{vrel} = w_v - w_w \cos\theta \approx w + V\theta - w_w. \quad (8)$$

The hydrodynamic forces on the dive planes associated with the controlled deflection of planes appears as $Z_{dp} \delta p$ and $M_{dp} \delta p$ in (6) and (7). [The hydrodynamic forces on the planes associated with vehicle angle of attack are subsumed along with hydrodynamic forces on other parts of the vehicle in the first two terms on the right sides of (6) and (7)]. The ACTV control law states the dive plane angle at a given time is proportional to the present depth and pitch errors:

$$\delta p = K_{\theta p}(\theta - \theta_{goal}) \quad (9)$$

where

$$\theta_{goal} = K_{zp}(z - z_{goal}).$$

After incorporating the transformation (8) and the control law (9), the system with forcing may be expressed as a single linear matrix differential equation:

$$\frac{d\mathbf{x}}{dt} = \mathbf{F}\mathbf{x} + \mathbf{D}_1 + \mathbf{D}_2 + \mathbf{G}\mathbf{v}, \quad (10)$$

where

$$\mathbf{F} = \begin{bmatrix} 0 & 0 & 0 & 0 & 0 \\ -Z_w & Z_w & Z_q + (m_L - m_T)V & -K_{zp}K_{\theta p}Z_{dp} & VZ_w + K_{\theta p}Z_{dp} \\ \frac{m_T}{m_T} & \frac{m_T}{m_T} & m_T & m_T & m_T \\ -M_w & M_w & M_q & -K_{zp}K_{\theta p}M_{dp} & VM_w + K_{\theta p}M_{dp} \\ \frac{J_y}{J_y} & \frac{J_y}{J_y} & J_y & J_y & J_y \\ 0 & 1 & 0 & 0 & 0 \\ 0 & 0 & 1 & 0 & 0 \end{bmatrix} \quad \text{and} \quad (11)$$

$$\mathbf{D}_1 = \begin{bmatrix} 0 \\ (mg - B) \\ \frac{m_T}{m_T} \\ \frac{BX_{CB}}{J_y} \\ 0 \\ 0 \end{bmatrix} \quad \mathbf{D}_2 = K_{zp}K_{\theta p}Z_{goal} \begin{bmatrix} 0 \\ Z_{dp} \\ \frac{M_{dp}}{J_y} \\ 0 \\ 0 \end{bmatrix} \quad \mathbf{G} = \mathbf{I}_5. \quad (12)$$

Equation (10) takes the form of (1) if the steady-state solution \mathbf{x}_{ss} is subtracted, where $\mathbf{F}\mathbf{x}_{ss} + \mathbf{D}_1 + \mathbf{D}_2 = 0$. Thus in the development of the smoother the system matrix \mathbf{F} of Eq. (11) is used. The lift and moment coefficients in \mathbf{F} are derived in appendix B.

The equations of motion for the AMTV are basically the same as for the ACTV, but in place of a simple proportional control system, the AMTV uses a proportional-plus-integral (PI) control system. This requires the addition of two state variables to the linear system to track the integrated depth error and integrated pitch error. The integrated errors are not computed from observations, but rather estimated and used by the filter. The AMTV state vector is

$$\mathbf{x} = \begin{bmatrix} w_w \\ w \\ q \\ z \\ \theta \\ z_{errint} \\ \theta_{errint} \end{bmatrix} = \begin{bmatrix} \text{vertical water velocity} \\ \text{vertical vehicle velocity} \\ \text{pitch rate} \\ \text{vehicle depth} \\ \text{vehicle pitch} \\ \text{integrated depth error} \\ \text{integrated pitch error} \end{bmatrix}. \quad (13)$$

It is a simple exercise to modify \mathbf{F} to incorporate the following PI control system (appendix B):

$$\delta p = K_{\theta p} \theta_{err} + K_{\theta i} \theta_{errint} \quad (14)$$

$$\theta_{err} = \theta - (K_{zp}z_{err} + K_{zi}z_{errint}) \quad (15)$$

$$\theta_{errint} = \int_0^t \theta_{err}(\alpha) d\alpha \quad (16)$$

$$z_{err} = z - z_{goal} \quad (17)$$

$$z_{errint} = \int_0^t z_{err}(\alpha) d\alpha. \quad (18)$$

Besides a seven-element state vector, the AMTV model differs slightly from the ACTV model due to the physical differences in mass, size, and control surfaces. The hydrodynamic coefficients for each vehicle are derived in appendix B.

d. System noise measurement parameters

It remains to specify \mathbf{G} , \mathbf{H} , \mathbf{Q} , and \mathbf{R} , as well as initial conditions for the state vector and \mathbf{P} . The choice of forcing and observed variables specifies \mathbf{G} and \mathbf{H} , which are matrices of ones and zeros. The initial state vector is chosen to be the zero vector, because the smoother uses an unbiased-state vector. As discussed above, the equation for the steady state can be subtracted from the equation of motion to produce the unbiased vector and equation in the form of Eq. (1).

The choice of \mathbf{Q} and \mathbf{R} is a long-standing problem in Kalman smoothing. A diagonal matrix \mathbf{R} consists of the variance of noise evident on the various measurement records multiplied by the time interval between measurements. This formulation of the noise arises as part of the derivation of the continuous Kalman filter from the discrete filter, which propagates variance. A discrete, purely random process with variance equaling σ_z^2 divided by the time step approximates the continuous white noise process of variance σ_z^2 in the limit of time step approaching zero (Gelb 1974, p. 121). To understand this, each discrete measurement can be viewed as an average of the continuous white noise process over the time interval. The variance of the average is the variance of the white noise process divided by the av-

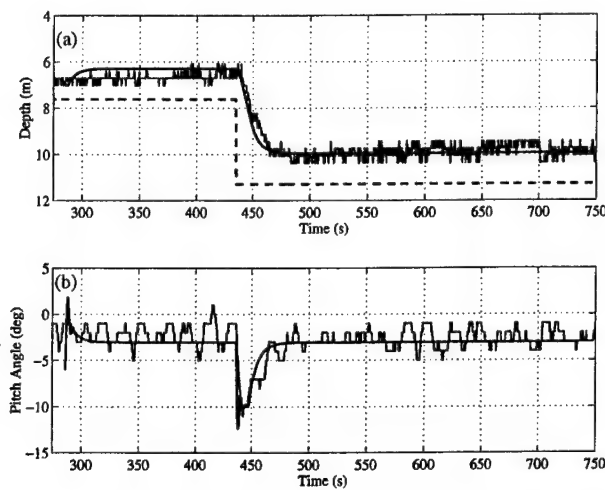


FIG. 4. Observed and simulated (a) depth and (b) pitch for the ACTV during a commanded depth change. The goal depth is indicated by the dashed line. The gray line indicates observed data. Because the dive plane angle is directly proportional to the depth error, and the vehicle is buoyant, it runs at a depth slightly offset from the goal. This run took place at lead 3 of LeadEx on 7 Apr 1992.

eraging interval (Jenkins and Watts 1968, p. 159). Therefore, the variance of the measurement noise is multiplied by the time step to get the corresponding variance of the idealized continuous measurement noise, \mathbf{R} . For the ACTV, only depth is measured so that \mathbf{R} is a scalar. The AMTV measurements include pitch rate, depth, and pitch, so \mathbf{R} is a 3×3 diagonal matrix.

The diagonal matrix \mathbf{Q} represents the random noise on the state vector. The vertical water velocity has random noise, but the only noise on the other state variables is due to the water velocity through the state equation. Therefore, elements of \mathbf{Q} are set at 10^{-10} except for $Q_{1,1}$, which is estimated from the variance of vertical water velocity measured independently by a turbulence mast when possible, or from the vertical velocity of the vehicle when necessary. The estimation of $Q_{1,1}$ from measurements of water velocity must be approached through the conversion process between discrete and continuous state models (Gelb 1974, 66–77). In the continuous model, the rate of change of the state is forced by the continuous white noise process, \mathbf{v} [Eq. (1)]. In the analogous discrete equation, the state itself is forced by a discrete process, which corresponds to the integral of the continuous forcing, \mathbf{v} , over the time step. The variance of the discrete forcing is just $\mathbf{Q}_k = \text{var}(\mathbf{v}_k)$. Taking the same variance expectation of the integral form and letting the time step approach zero gives $\mathbf{Q}_k = dt \times \text{var}[\mathbf{v}(t)] = dt \times \mathbf{Q}$ to first order. As a net result, $Q_{1,1}$ is equal to the variance in measured (discrete) water velocity divided by the filter time step.

The choice of \mathbf{P}_0 and derivation of \mathbf{P}_f are done in the process of filtering. For a time-invariant system such as this, \mathbf{P}_f tends to a steady-state value (Gelb 1974, p. 142). Here we integrate (4) and (5) using an ODE solver with an arbitrary \mathbf{P}_0 until a steady-state \mathbf{P}_f is found, then

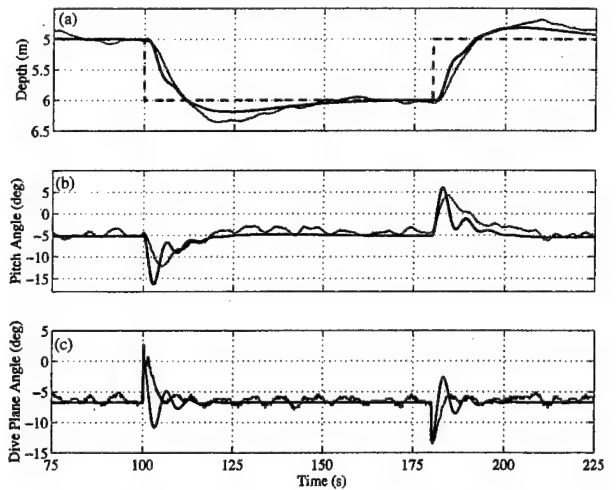


FIG. 5. Observed and simulated (a) depth, (b) pitch, and (c) dive plane angle for the AMTV during a commanded depth change for run 3 at SHEBA on 7 Aug 1998. The dashed line is the goal depth, and the gray line indicates observed data. The modeled dive plane angle has been offset by 3.5°, to match the observed value, which is difficult to calibrate to this accuracy.

restart with the new value of \mathbf{P}_0 equal to the steady-state \mathbf{P}_f .

e. Model and smoother tests

The vehicle system models were first tested by comparing simulations against measured responses to commanded step changes in run depth. Figure 4 shows such a comparison for ACTV depth and pitch, using the model of Eqs. (6)–(12). In this paper, depth and velocity are positive downward. The run data were obtained from LeadEx on 7 April 1992. Besides a start-up transient in the model, the depth and pitch are modeled well through both the commanded depth change and in steady state.

The analogous test of the AMTV model (Fig. 5) shows agreement between the modeled and actual depth, pitch, and dive plane angle. These run data were obtained at ice station SHEBA on 7 August 1998. On average the simulated and actual run depths agree well, though the depth response of the model to step change depth commands is slightly faster than the actual vehicle response initially and then tends to undershoot slightly. It should be noted that in applying the Kalman technique, only portions of a run where the vehicle was running straight and level will be analyzed. Depth excursions during these segments are much smaller than the commanded depth changes. Thus, the step responses of Figs. 4 and 5 are extreme tests and may force the model beyond the region where the linearized model is strictly appropriate. The model is likely to be more accurate for smaller deviations from steady state.

We investigate the extent to which the ACTV moves with the water by forcing the vehicle model with a time series of actual vertical velocity measured by a TIC at LeadEx. To force the model, the TIC data are translated

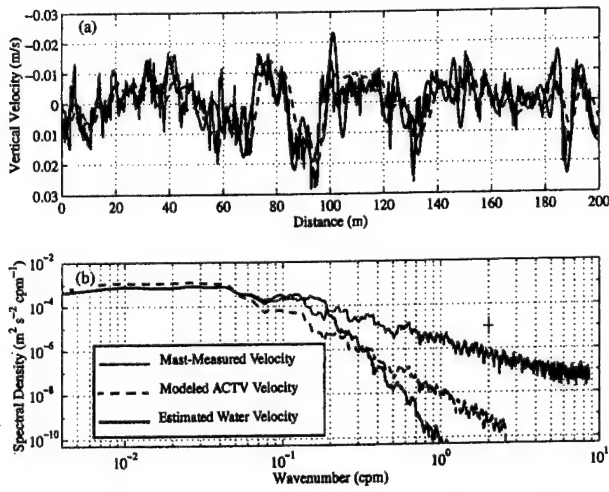


FIG. 6. (a) The vertical water velocity measured by a turbulence frame at lead 3 of LeadEx (gray line) was used to force the model ACTV, whose vertical velocity is plotted (dashed line). Shown with a black line is the Kalman smoother estimate of vertical water velocity, based only on the depth of the model ACTV plus Gaussian noise. (b) The wavenumber spectra of the series show the vehicle roughly follows vertical water velocity at scales greater than 15 m, and the smoother estimate agrees with the original forcing at all wavenumbers below 0.2 cpm (scales greater than 5 m). The spectra were calculated using the multitaper method with NW = 6 and by averaging the first 6 eigenspectra. The length of the 95% confidence interval and resolution bandwidth are shown as a criss-cross in the upper right (as in Percival and Walden 1993, p. 343).

from a measurement in time to a measurement in space using Taylor's hypothesis. We then model the ACTV traveling through this turbulent field. The vertical water velocity (solid gray) and modeled vertical ACTV velocity (dashed) are shown in Fig. 6a, and Fig. 6b shows their wavenumber spectra. The simulated vertical velocity of the ACTV roughly agrees with the water velocity. This supports the idea of MM98 that the ACTV tends to track vertical water motion at the scales of boundary layer turbulence. Besides rolling off at a high wavenumber, the modeled vehicle velocity also is affected by the control system at low wavenumbers, but at the low frequencies involved, the effect on vertical velocity is small.

To test the Kalman smoothing algorithm and demonstrate that it improves estimates of vertical water velocity, the vehicle data simulated above are complimented with artificial noise and used as smoother input to recreate the forcing function. This recreation is then

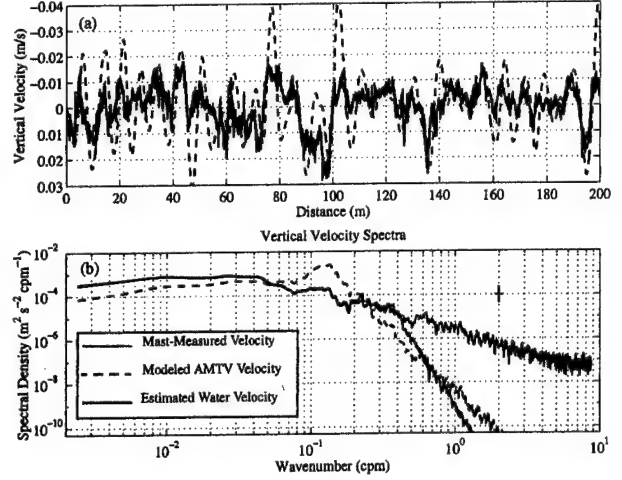


FIG. 7. Same as Fig. 6, except for the AMTV. Note the spectrum of the smoother estimate of vertical water velocity agrees with that of the forcing velocity at all wavenumbers below 0.4 cpm.

compared with the water velocity record that forced the model. For the ACTV test the modeled vehicle depth is used, and to it Gaussian noise is added to resemble the ACTV pressure sensor noise. Here \mathbf{R} is the variance of this noise multiplied by the time interval, and is given in Table 1. The smoother uses this artificial depth measurement in the smoothing algorithm [Eqs. (4), (5), (A4), (A5)] to estimate vertical water velocity. The variance of the water velocity forcing, $\mathbf{Q}_{1,1}$, is set based on the water velocity forcing the model and is also in Table 1. In Fig. 6 the Kalman smoother estimate of the water velocity (solid black) is compared to the water velocity that forced the model (solid gray). The smoother recovers the water velocity from the modeled vehicle depth out to a wavenumber of about 0.2 cycles per meter (cpm), or a 5-m wavelength.

The identical procedure was carried out with the AMTV model. The smoother was applied to the depth simulated by the AMTV model, and the resulting water velocity estimate is plotted in Fig. 7. See Table 1 for smoother parameters. The larger AMTV did not follow the water velocity as closely as the ACTV (Fig. 7a). However, when the smoother is used, the more accurate pressure sensor of the AMTV compensates for this and the forcing signal is recovered more accurately. The spectra of the true and estimated vertical water velocity (Fig. 7b) agree down to a wavelength of less than 3 m

TABLE 1. Kalman smoother parameters for three test cases: variance of measurement noise (\mathbf{R}) and variance of vertical water velocity (\mathbf{Q}).

ACTV Figs. 6, 9–13	AMTV 1 Fig. 7	AMTV 2 Figs. 8, 14–16
$\mathbf{R} = dt * \text{diag}(\sigma_i^2)$ $dt \sim 0.12 \text{ sec}$	$\sigma_i^2 = (0.015 \text{ m})^2$	$\sigma_i^2 = (0.005 \text{ m})^2$
$\mathbf{Q}_{1,1} = dt^{-1} * \sigma_{ww}^2 \quad (\text{m}^2 \text{ s}^{-3})$	6×10^{-4}	3×10^{-4}

$$\begin{aligned}\sigma_g^2 &= (0.1 \text{ deg s}^{-1})^2 \\ \sigma_z^2 &= (0.005 \text{ m})^2 \\ \sigma_\theta^2 &= (0.1 \text{ deg})^2 \\ &3 \times 10^{-4}\end{aligned}$$

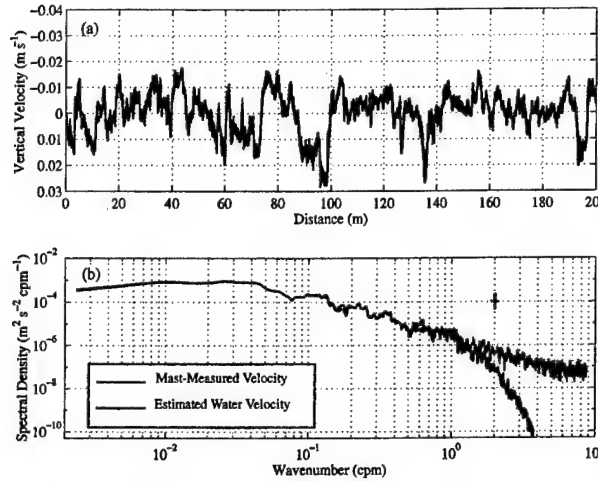


FIG. 8. As in Figs. 6 and 7. Vertical water velocity estimated from the modeled depth, pitch, and pitch rate of AMTV. Modeled vehicle velocity is identical to that in Fig. 7, and is not shown here. Prior to smoothing, Gaussian noise sequences were added to each observed variable. More observed variables results in a better water velocity estimate, whose spectrum agrees with the original forcing function spectrum at all wavenumbers below about 2 cpm.

(wavenumbers below 0.4 cpm). The improvement is over the range of wavenumbers where vehicle dynamics are expected to cause the vehicle velocity to deviate from the water velocity. The oscillatory roots of Eq. (10) for the AMTV (the complex eigenvalues of \mathbf{F}) correspond to periods of 6.5 and 140 s, or assuming a vehicle velocity of 1.1 m s^{-1} , wavenumbers of 0.14 and 0.0065 cpm. The former root is dominant and is likely responsible for the peak in the vehicle velocity spectrum above 0.1 cpm. The smoother corrects for the vehicle motion at this wavenumber, resulting in an accurate estimation of the forcing function.

The AMTV smoother test was repeated using the simulated vehicle pitch rate, pitch, and depth, rather than only depth. Noise was added to each before going into the smoother. Figure 8 shows improvement in the vertical water velocity estimate for higher wavenumbers. The smoother-derived vertical velocity agrees with the true forcing out to almost 2.0 cpm (Fig. 8b).

It is important to realize that the real vehicle will not respond as the model responds to fluctuations of wavelength smaller than about 1.6 m. For both the ACTV and AMTV models, the water velocity is assumed uniform over the length of the vehicle. In practice, for variations in w_w at wavelengths much less than the hull length, the net effect on vertical motion of the vehicle is small. Vehicle motion at wavelengths near the hull length may be strongly affected by horizontal gradients in velocity. MM98 suggested that this may result in a gradient-pitching phenomenon that would amplify the vehicle response. As the vehicle moves into a region of rapidly increasing w_w (positive down) the front of the vehicle is affected first, and the vehicle will pitch down so as to amplify the depth response.

As will be discussed, the gradient-pitching phenomenon appears to be detectable in the AMTV data. Therefore an effort has been made to account for the horizontal gradient of w_w over the length of the vehicle. Our method is to include horizontal variability in the equation of the system state. The state vector [Eq. (13)] and the corresponding system matrix, \mathbf{F} , are modified so that w_w is replaced by w_f , the water velocity acting on the front of the vehicle, and w_b , the water velocity acting on the back of the vehicle. The velocity w_b is a lagged version of w_f approximated by a first-order process with time-constant τ driven by w_f that is forced by white noise. The time domain w_b for a single step in w_f is

$$w_b(t) = 1.58w_f(t_i) \left\{ 1 - \exp \left[-\left(\frac{t - t_i}{\tau} \right) \right] \right\}. \quad (19)$$

The proportionality constant is set so that for a step change in w_f , the amplitude of the velocity at the back of the vehicle, w_b , at time $(t_i + \tau)$ is equal to the velocity at the front of the vehicle at time t_i . The value of τ is set to 1.5 s, about the time it takes for the AMTV to travel its own hull length. The vertical water velocity estimate is for w_f . Details are left to appendix B.

3. Field test results

To illustrate the utility of the Kalman smoothing method, we have used it to analyze ACTV and AMTV data from three experiments, LeadEx, ANZFLUX, and SHEBA.

a. Arctic Lead Experiment (LeadEx)

During LeadEx the ACTV made horizontal profiles of conductivity, temperature, and depth under newly formed leads in the sea ice (LeadEx Group 1993; MM98). Instrument huts were flown to leads near a central camp, which was initially at $72^{\circ}47'N$, $144^{\circ}W$ on 12 March 1992. The data were taken under and around these rapidly freezing gaps in the pack ice. Upon contact with the cold air, the seawater begins to freeze, rejecting salt, and eventually releasing dense, high salinity water (Wettlaufer et al. 2000). This results in free convection when ice velocities are low and forced convection if ice velocities are high. The data in this section were taken at lead 3: a wide (1000 m) lead with a reasonably high ice–water-relative velocity of 0.11 – 0.13 m s^{-1} . A TIC mast was fixed to the ice at the downstream edge of the lead and under these conditions provided reliable turbulence data with which to compare the Kalman smoother results.

The sample of vehicle data shown in Fig. 1 was gathered during run 4 at lead 3. The ACTV was traveling 1.7 m s^{-1} at about 15-m depth during this run and collecting data at 9 Hz. Detrended temperature, T' , and salinity S' , have been smoothed with a 1-m horizontal bin average. Vertical vehicle velocity in the third panel

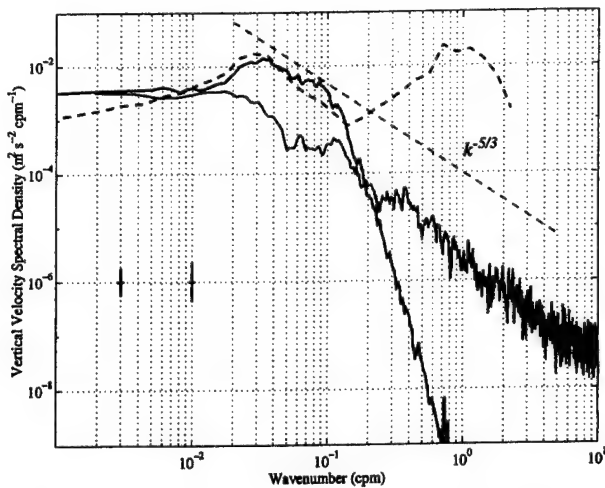


FIG. 9. Vertical velocity spectra from lead 3, run 4 of LeadEx. The smoothed average of vertical vehicle velocity spectra from ACTV leg 2 and leg 3 is shown as a dashed black line, while the average of the vertical water velocity spectra from the same 2 legs calculated by the Kalman smoother is the solid black line. The solid gray line represents the spectrum from the turbulence mast. Both instruments were taking data simultaneously: the ACTV at 15-m and the mast at 14-m depth. The ACTV was in the lead during leg 2 and half of leg 3, while the mast was at the downstream edge of the lead. A 95% confidence interval for the mast spectrum is the gray vertical bar, and the confidence interval for the vehicle-derived water velocity is the black vertical bar. A $k^{-5/3}$ line is also shown (dashed gray).

was calculated by differentiating the depth record and smoothing with a 5-m bin average. Vertical water velocity for the run has been calculated with the Kalman smoother using the vehicle model of Eqs. (9)–(12) and is shown in the fourth panel. Note the similarity to the vehicle velocity. The horizontal profiles of turbulent flux were calculated using w_w , S' , T' , and a mean density and heat capacity: $F_{\text{heat}} = \rho C_p w_w T'$ and $F_{\text{salt}} = \rho w_w S'$. These are shown in the fifth and sixth panels respectively. The sign convention for vertical water velocity, and therefore heat and salt flux, is positive downward. The vertical axes of the plots have been oriented accordingly. Turbulence frame measurements at 14-m depth during the same period of time included vertical water velocity, temperature, and salinity.

The wavenumber spectra of vertical velocity obtained from the TIC and from the Kalman smoothed ACTV data are compared in Fig. 9. The time series gathered by the TIC has been translated into a spatial series using the mean ice velocity (10 cm s^{-1}) and sampling frequency (0.5 Hz). The frame-derived vertical water velocity shows the wavenumber, k , rolls off with a slope of $k^{-5/3}$, indicative of the inertial subrange for turbulence. The vertical vehicle velocity spectra for the segments of run 4 under lead 3 are averaged and smoothed in Fig. 9 (dashed line). The average of the spectra of the water velocity for 2 segments of ACTV run 4 at lead 3 is also plotted (solid black line). Despite the aggressive filtering of high-frequency oscillations, spikes were evident in the smoothed water velocity spec-

trum at a fundamental wavenumber of 0.13 cpm and higher harmonics. The spikes every 4 s carried through from the raw depth record acquired by the vehicle and are due to the interference of the acoustic transducer. Peaks in the wavenumber spectra at the harmonics of the spike frequency were found to be significant with Thomson's F-test for periodicity (Percival and Walden 1993, 496–501). Because only the background spectrum is of interest and not the spectral peaks, the peaks have been removed.

The smoother-derived water velocity agrees with the turbulence frame at wavenumbers below 0.01 cpm and in the region around 0.2 cpm. The smoother is accounting for the control system at low wavenumbers, and for measurement noise at high wavenumbers. The smoother-derived energy is a factor of 9 higher than the TIC spectrum between 0.02 and 0.1 cpm. Similar bulges occur in every ACTV spectrum from LeadEx. A hump in filtered vehicle velocity around 0.03 cpm is also present in MM98 (their Fig. 9a). It is narrower, but about an order of magnitude above the frame levels. The peak is likely due to an unrecognized mode of vehicle motion that is not corrected for properly with the Kalman smoother. MM98 show that (their Fig. 9a) the vertical water velocity (filtered ACTV velocity) spectrum stays close to the frame spectrum at higher wavenumbers where the filter is active. In this, the ad hoc filter of MM98 does a slightly better job than the Kalman smoother because the MM98 filter was designed by matching ACTV and TIC spectra. The advantage of the Kalman smoother in this situation is that by being based only on an a priori derivation of the vehicle dynamics, its results are an independent description of the turbulent boundary layer. Therefore, in complex situations boundary layer features such as horizontal inhomogeneity are unlikely to be obscured by mechanistically constraining the AUV results to agree with the fixed sensors.

The smoother drastically reduces the energy in vehicle velocity above 0.25 cpm. The ACTV model used by the smoother has its only complex eigenvalue (or characteristic frequency) at 0.014 cpm, so at much higher wavenumbers, vehicle dynamics cannot account for large fluctuations in the vehicle velocity. The high-wavenumber energy in vehicle velocity is due to sensor noise that the smoother filters.

Even though the vertical water velocity spectrum is imperfect, the heat and salt fluxes estimated with the ACTV compare favorably with the TIC measurements. The heat and salt fluxes from the TIC and ACTV are not expected to be identical because of the episodic nature of the turbulence and because the TIC sampled at the lead edge while the ACTV sampled under and around the lead. However, as shown in Fig. 10, the spectra of heat and salt flux from the ACTV compare well to those of the TIC. The broad peak around 0.02 to 0.1 cpm in vertical water velocity has not carried through to the flux calculations. This is because the erroneous velocity fluctuations in this wavenumber

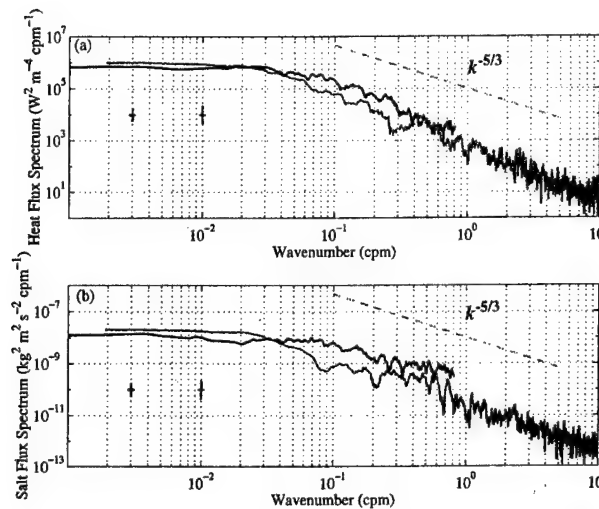


FIG. 10. As in Fig. 9, except for vertical (a) heat flux and (b) salt flux. The gray lines are the spectra for fluxes calculated using turbulence frame data. Each black line is the average of 2 ACTV flux spectra from the 2 segments of run 4 in the lead.

range are not coherent with temperature and salinity fluctuations. The average flux results are also gratifyingly similar. The heat flux averages for the ACTV (legs 2 and 3 of run 4 at lead 3) under the lead upstream of the TIC are 92 and 54 W m^{-2} . The TIC average over the same period is 78 W m^{-2} . Salt flux averages are 1.5 and $1.1 \times 10^{-5} \text{ kg s}^{-1} \text{ m}^{-2}$ for the ACTV and $0.58 \times$

$10^{-5} \text{ kg s}^{-1} \text{ m}^{-2}$ for the TIC. Temperature and salinity in both datasets are found to be significantly correlated with vertical water velocity by using the empirical probability distribution function for correlation at random lags as in MM98, Fleury and Lueck (1994), and Lueck and Wolk (1999). A correlation is considered significant if it is above the 2 standard deviation level for the distribution of correlation coefficients at random lags.

b. Antarctic Zone Flux Experiment (ANZFLUX)

The ANZFLUX experiment (McPhee et al. 1996) has provided the opportunity to test the Kalman smoother method with data from a different boundary layer regime. It took place during the southern winter of 1994. The goal of the experiment was to measure turbulent fluxes in the high heat flux region of the Weddell Sea. Two 6-day manned ice drift experiments were conducted. The ACTV was deployed during the second manned experiment over Maud Rise.

The relatively long run analyzed here (run 3) was carried out on 5 August 1994 (day 217) at 0917 local time. A storm caused ice velocities of up to 0.45 m s^{-1} late on day 216, while during the run early on day 217, the ice had slowed to 0.14 m s^{-1} . A box pattern at 50-m depth was run, and a lead was intersected midway through. The three-dimensional run track is shown in Fig. 11 with heat flux overlaid. The heat flux was estimated using the temperature fluctuations and Kalman

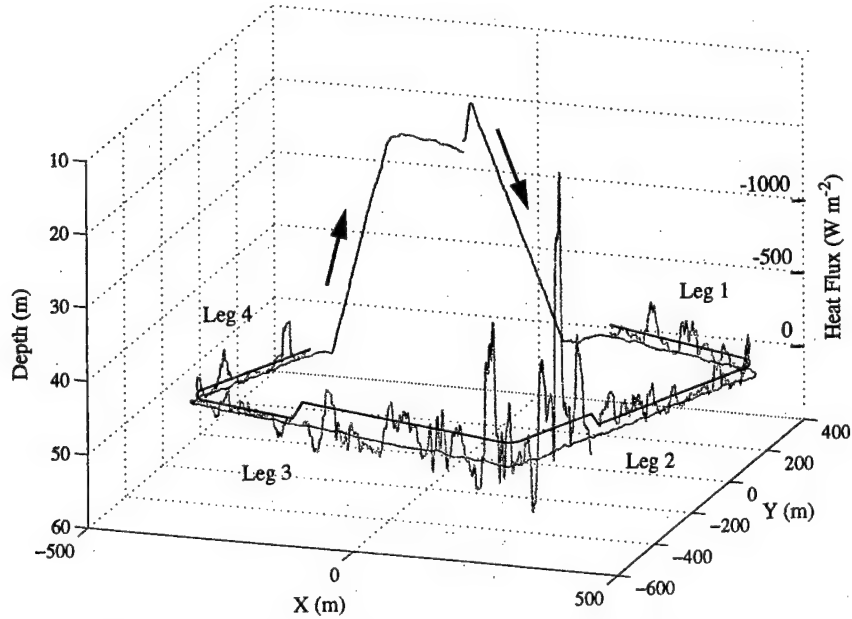


FIG. 11. Three-dimensional track of the ACTV during run 3 of ANZFLUX on 5 Aug 1994. The vehicle starts at about 15-m depth, dives to 50 m and executes a clockwise box pattern. The heat flux calculated from the ACTV motion and temperature probe is plotted in light gray, and the mean heat flux for three different regions is in black. The lead is located in the nearest corner, where there is a strong upward mean heat flux of -145 W m^{-2} . Leg 1 and the first part of leg 2 average -64 W m^{-2} , and the last part of leg 3 and leg 4 average -30 W m^{-2} . The heat flux has been smoothed with a 20-m running average.

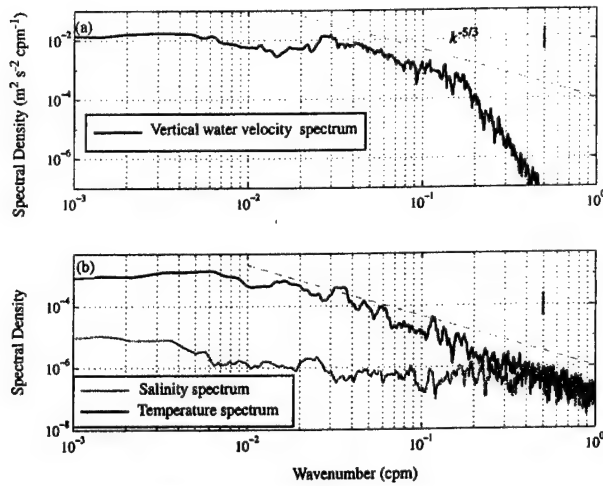


FIG. 12. (a) Vertical water velocity spectrum and (b) temperature and salinity spectra for ANZFLUX run 3, edges 2 and 3 of the box pattern (under the lead). The dashed gray lines obey the $k^{-5/3}$ law. The velocity and temperature spectra show a clear inertial subrange, but the salinity spectrum (gray solid line) does not. 95% confidence limits for the spectral estimation are shown.

smoother derived vertical water velocity. The average heat flux in three regions is also plotted.

Spectra of Kalman smoother-derived vertical water velocity, temperature, and salinity from ANZFLUX ACTV data are shown in Fig. 12. The spectrum of the

vertical water velocity fluctuations varies as $k^{-5/3}$ in a broad inertial subrange between 0.03 and 0.2 cpm. The spectrum does not display the hump in energy between 0.02 and 0.1 cpm that is apparent in the LeadEx data (Fig. 9). This may be because the model best matches the 1994 vehicle configuration. As with the LeadEx data, narrow peaks in the vertical water velocity spectrum caused by acoustic transducer spikes in the depth data have been removed in Fig. 12. These spikes are uncorrelated with temperature and salinity, so they do not contribute to the mean heat or salt flux estimates. The temperature spectrum shows an inertial subrange for wavenumbers above about 0.02 cpm (Fig. 12b). The energy in salinity is low and nearly independent of the wavenumber, indicating that salinity flux is not a factor in the turbulence.

The horizontal profiles help illustrate boundary layer conditions (Fig. 13). Vertical water velocity is energetic everywhere. Large temperature spikes are present under the lead region while salinity is relatively quiet everywhere. The instantaneous heat flux is large upward in the lead region (-145 W m^{-2} average) and smaller upward away from the lead (-30 to -64 W m^{-2} average). The salt flux is quite small everywhere ($0.13 \times 10^{-5} \text{ kg s}^{-1} \text{ m}^{-2}$ average). Temperature and velocity are significantly correlated in the lead ($R = -0.21$), while the correlation between salinity and vertical water velocity is not significant in the lead ($R = 0.06$). Corre-

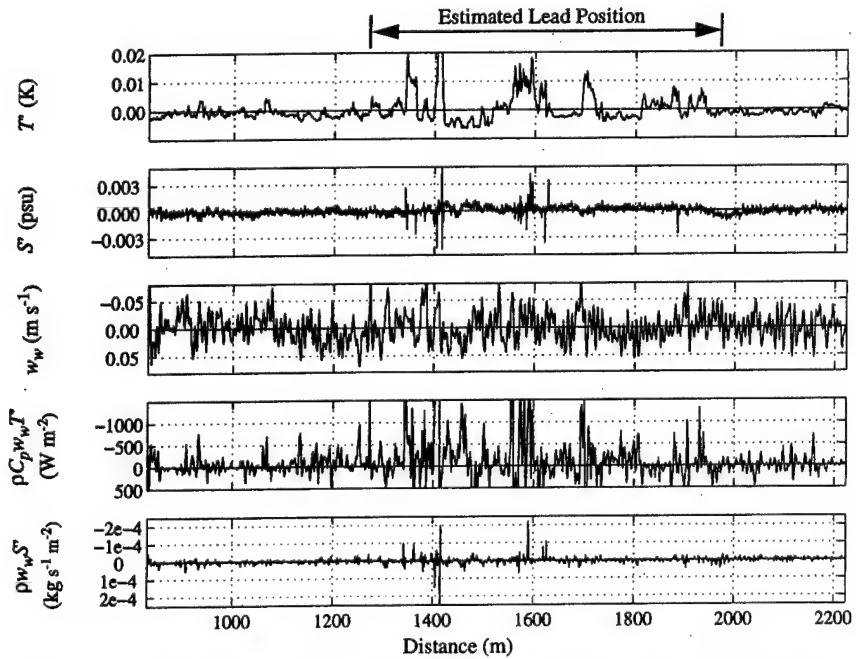


FIG. 13. ACTV data from run 3, legs 2 and 3 of ANZFLUX. Vehicle speed was 1.8 m s^{-1} ; depth was 50 m, and mean ice-ocean relative velocity was 0.14 m s^{-1} . The data have been smoothed with a 1-m bin average. The mean heat flux between the 1300- and 2000-m marks (the central region of Fig. 11 and estimated lead position) is -145 W m^{-2} . The correlation coefficients in this region for temperature and salinity with velocity are -0.21 and 0.06 , respectively. The latter is not significantly different from zero. All scales are the same as Fig. 1.

lation coefficient significance was tested using the same method described in section (3a).

There were no fixed masts or other measurements at the lead; the vehicle ran beyond the domain of most of the other ANZFLUX measurements. However, the ACTV results show good agreement with boundary layer conditions we expect on the basis of theory and bulk flux estimates at the surface. The heat flux from the open lead to the atmosphere was calculated to be 196 W m^{-2} upward using bulk formulas from Ruffieux et al. (1995; meteorological data courtesy of P. Guest 1999, personal communication). This is roughly in accord with our measurement of -145 W m^{-2} upward at 50 m below the surface of the lead. Heat flux to the atmosphere over the ice was about 20 W m^{-2} upward during this time (Guest 1998). The flux from the ocean to the ice was about 25 W m^{-2} (McPhee 1999) corresponding to the $30-64 \text{ W m}^{-2}$ upward heat flux at 50 m estimated from the ACTV. Our interpretation is that the boundary layer was being well mixed by motion of the ice. Heat was being drawn upward from and through the mixed layer in rough proportion to the surface flux. Buoyancy-driven convection was not a factor under the lead because in spite of freezing air temperatures, the heat flux from the ocean was sufficient to prevent freezing of the lead surface. Indeed, the lead remained open throughout the drift (M. G. McPhee and T. Lehman, 1994, personal communication). The bottom melting suggested by the 5 W m^{-2} difference between ice-air and ocean-ice heat flux was too small to significantly stabilize the boundary layer at the time of the run. Because the salt flux was small and temperature had little effect on density near the freezing temperature, the buoyancy flux, $g\rho^{-1}\langle\rho'w_w\rangle$ was small and had little effect on the turbulence or circulation. For the observed fluxes, the ratio of the pressure gradient to the shear stress terms in the mean momentum equation, or lead number, L_0 , (Morison et al. 1992) was much less than 1, meaning the shear stress dominated the buoyancy forces. This is in contrast to lead 3 of LeadEx for which L_0 was between 0.32 and 0.96 (MM98), and for which McPhee and Stanton (1996) showed that shear and buoyant production of turbulent kinetic energy were of the same order.

c. Surface Heat Balance of the Arctic Ocean (SHEBA)

As described by Moritz and Perovich (1996), the overarching goal of SHEBA was to improve our understanding of the local-scale processes in order to produce accurate global climate models and learn the role of the Arctic in global climate change. Our work focused on a summer lead study to measure the partitioning of solar insolation into edge melting, basal melting, and raised mixed layer temperatures. In contrast to the winter, the water input to the surface in the summer is fresher and therefore less dense than the ambient water because it consists of melted ice and snow. The fresh

meltwater tends to suppress turbulence generated by wind and ice motion. On a fundamental level, the summer lead study will aid in understanding the stably stratified, horizontally varying boundary layer.

The role of the AMTV was to gather horizontal profiles of temperature and salinity variations in order to calculate heat and salt fluxes under varying surface conditions (observed by an upward-looking altimeter on the AMTV that measured the ice draft). The mode of operation was similar to that of LeadEx. The AMTV was lowered through a hole drilled a few meters from the lead edge. Four tracking hydrophones were lowered to 15-m depth in locations 50–100 m apart. A mast with a TIC of M. McPhee was placed in the water at the downstream edge of the lead. The mast was typically at the same or slightly shallower depth as the AMTV. Runs were planned such that the AMTV would cross the lead edge in the upstream and downstream directions, sampling water approximately in the path of the frame.

Forty-four runs adding up to 70 km of run track were gathered between 11 July and 7 August 1998. During this time, the station drifted with the ice pack from 78.1°N , 167°W to 78.4°N , 159°W . Data from 7 August (day 219) will be used here to discuss the performance and utility of the instrument and method because conditions were optimum for comparisons between the AMTV and TIC results: the lead upstream of the mast was over 1 km wide, the radiative fluxes were strong, the wind speed was 14 knots, and the ice-ocean relative velocity was 0.15 m s^{-1} . The AMTV went back and forth across the lead edge parallel or antiparallel to the relative surface current at about 5-m depth. The vehicle speed was approximately 1.1 m s^{-1} . Observations of vehicle depth, pitch rate, and pitch were used in estimating vertical water velocity, along with the parameters in Table 1. The heat flux was calculated using the Kalman smoother-estimated vertical water velocity and temperature fluctuations. Also on day 219, the TIC was placed a meter or so out from the ice edge with the instrument cluster at 5-m depth. It gathered temperature, conductivity, and vertical water velocity fluctuations over four 60–100-min periods that overlapped the 4 AMTV runs.

For each instrument, vertical water velocity spectra from data on 7 August 1998 are averaged and compared (Fig. 14). Four TIC spectra are averaged, and seven AMTV spectra from the under-lead segments are averaged. The estimate that uses the single-point water velocity model [state variables in Eq. (13) only] is flawed by 2 humps centered at 0.08 and 0.3 cpm. The excess energy at 0.3 cpm led us to believe that the gradient pitching phenomenon discussed earlier could be responsible. By accounting for the pitching moment due to water velocity variation across the vehicle length [see Eq. (19) and appendix B for a discussion of the model improvement], the new model produces an estimate without the broad peaks at 0.08 cpm and 0.3 cpm.

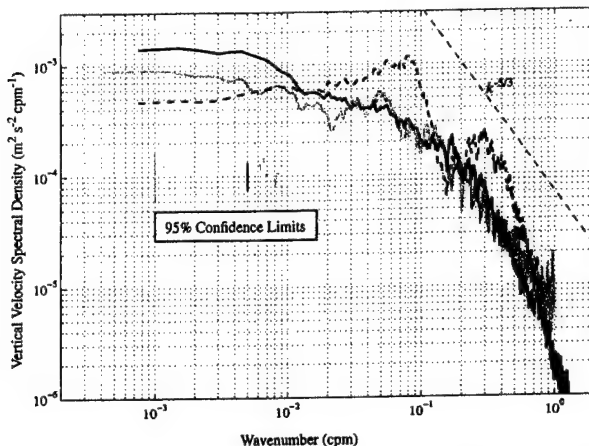


FIG. 14. Vertical water velocity spectra for data at 5-m depth on 7 Aug 1998 (day 219) at the SHEBA experiment site. The solid black line is an average of 7 spectra from different segments of 4 AMTV runs between 1300 and 2000 local time (8 h behind UTC). The dashed line shows the result before the model was modified to allow for different water velocities at the front and rear of the vehicle. The solid gray line is an average of the four TIC records taken during the same period downstream of the AMTV segments. Thin vertical bars show the 95% confidence intervals for the AMTV spectra (black) and the mast spectrum (gray).

The vertical water velocity spectrum estimated using the revised model shows excellent agreement with the turbulence mast spectrum, the 95% confidence intervals for the spectral estimation overlapping each other at all wavenumbers.

The Kalman smoother results shown in Fig. 14 are based on vehicle model coefficients derived from bench calibrations, general empirical data, and vehicle dynamics. In the course of debugging the Kalman smoother we examined the sensitivity of the smoother results to errors in vehicle model coefficients. A factor of 2 error in the model feedback coefficient for dive plane deflection relative to pitch error resulted in an estimated velocity spectrum about a factor of 4 less than the TIC spectra in a notch from 0.08 to 0.12 cpm. Moving the model hydrodynamic center of pressure on the hull 10 times farther forward and increasing the vehicle moment of inertia 25% resulted in a factor of 3 reduction in the velocity spectrum between 0.02 and 0.09 cpm. Increasing the model lift coefficient of the dive planes 50% decreased the velocity spectra a factor of 2 between 0.1 and 0.15 cpm while it raised the spectra a factor of 2 at wavenumbers below 0.01 cpm. Increasing the overall heave damping coefficient [Z_w , Eq. (B6)] 50% increased the velocity spectrum a factor of 2 below 0.06 cpm. Typically, coefficient errors of 50% resulted in localized, factor of 2–3 spectral errors. From this we suggest the Kalman smoothing approach is robust to model coefficient errors less than 10% and produces reasonable results for errors as high as 50%. It is noteworthy that the factor of 2 error in the dive plane feedback coefficient produced negligible change in the model step response shown in Fig. 5. Thus comparison of smoother-

derived spectra with independently measured velocity spectra may be better than examining vehicle step responses for disclosing small errors in model parameters. This is probably because the energy levels revealed in the spectra are much finer than and rely on more data than typical step-response diagnostic vehicle maneuvers.

The utility of the Kalman smoother applied to the AMTV is best illustrated by examining a single run in detail. Run 2 was completed at 1600 local time on day 219 (0000 UTC day 220), and a portion of the data is shown in Fig. 15. The scale of each subplot is the same as Figs. 1 and 13 except the salinity deviation scale is 3 times larger, and the salt flux scale is half the size. The uppermost plot displays the ice draft measured by the acoustic altimeter on the AMTV along with temperature deviations. Salinity deviations are in the second panel. Both temperature and salinity fluctuations weaken within about 100 m downstream of the lead edge. The vertical water velocity [estimated using the improved model (B13)–(B14)] is the third panel down, and it is less energetic than the 2 winter lead experiments, likely due to the stable stratification. The magnitude and length scale of the velocity fluctuations appear to increase downstream of the lead, in contrast with the temperature and salinity fluctuations that become less energetic. The series of heat and salt flux across the lead and ice edge are shown in the fourth and fifth panels. Heat and salt fluxes are averaged over 100-m blocks: each average is shown as a solid line over the averaging domain. This averaging interval is chosen because it is likely to include several eddies of the dominant scale. A spectrum of vertical velocity plotted in an energy-preserving representation [kS vs $\log(k)$] shows a peak at a wavenumber around 0.1–0.2 cpm, so the size of the most energetic eddies was around 5–10 m. Fresh, warm water was being mixed downward in the lead, with a particularly strong event between the 1200- and 1300-m mark. For the entire lead segment shown, the average heat flux was 87 W m^{-2} (downward), and the average salt flux was $-0.41 \times 10^{-5} \text{ kg s}^{-1} \text{ m}^{-2}$ (upward). The 100-m block averages range from a heat flux of 36 – 214 W m^{-2} and a salt flux of -0.03 to $-0.88 \times 10^{-5} \text{ kg s}^{-1} \text{ m}^{-2}$. The other lead segment (AMTV moving away from the ice) at 5-m depth for this run yields a heat flux of 92 W m^{-2} , and the salt flux is not available due to a nonlinear drift in conductivity. Under the ice, the first 100-m block indicates fluxes of the same magnitude and in the same direction as in the lead (87 W m^{-2} and $-0.5 \times 10^{-5} \text{ kg s}^{-1} \text{ m}^{-2}$). The heat flux changed sign in the next downstream segment under the ice (-21 W m^{-2}), but the salt flux continued to be strongly upward ($-1.1 \times 10^{-5} \text{ kg s}^{-1} \text{ m}^{-2}$). Average fluxes of 20 W m^{-2} and $-0.9 \times 10^{-5} \text{ kg s}^{-1} \text{ m}^{-2}$ were observed for the entire under-ice portion of Fig. 15. The role of the ice edge seems to be important, and has yet to be investigated satisfactorily.

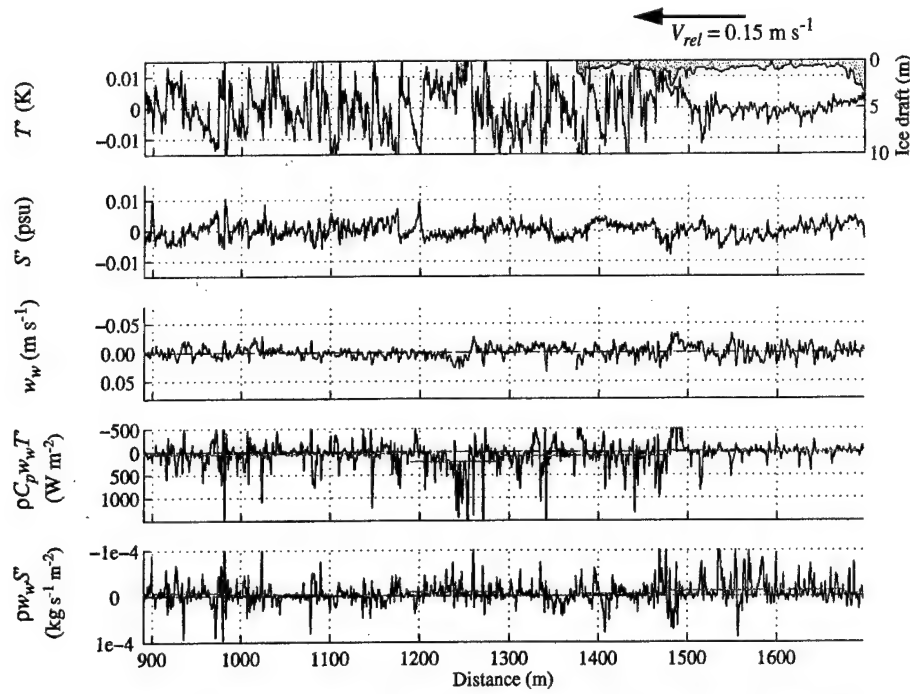


FIG. 15. AMTV data from run 2, legs 2 and 3 of SHEBA on 7 Aug 1998. Vehicle speed was 1.1 m s^{-1} , and depth was 5 m. Ice draft (from an acoustic altimeter) and mean ice-ocean relative velocity (0.15 m s^{-1}) are indicated. The data have been smoothed with a 1-m bin average. Mean fluxes in horizontal bins 100 m wide are indicated by the solid horizontal lines. In the lead the heat flux is 87 W m^{-2} (downward), and the salt flux is $-0.41 \times 10^{-3} \text{ kg s}^{-1} \text{ m}^{-2}$ (upward). Note the full scale on each plot is the same as Figs. 1 and 13, except for the salinity scale, which is 3 times larger here, and the salt flux scale, which is half the size.

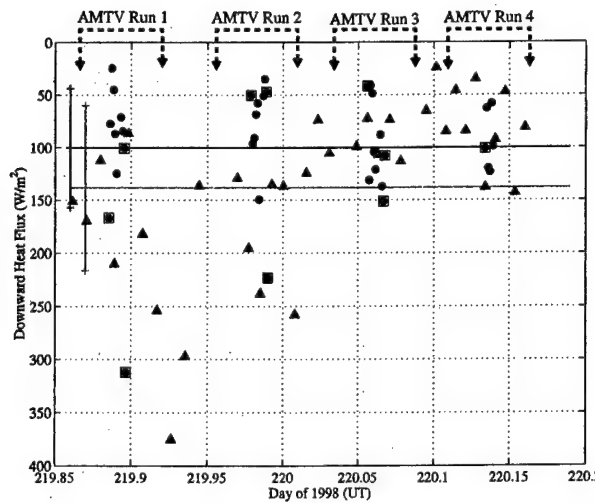


FIG. 16. Vertical heat flux at SHEBA on 7 Aug 1998 for the AMTV (circles) and the TIC (triangles). Each point represents a spatial average of 100 m (90 s of AMTV data or 11.1 min of TIC data), placed at the time of the center of the averaging interval. Only AMTV segments from in the lead upstream of the mast are plotted. AMTV blocks that are centered within 200 m of the ice edge are indicated by a box around the data point. The averages for the day are indicated by the horizontal lines, and the vertical bars indicate 1 std dev in either direction. The TIC averaged 138 W m^{-2} with a std dev of 78 W m^{-2} (gray) and the AMTV averaged 100 W m^{-2} with a std dev of 57 W m^{-2} (black).

The vertical heat and salt flux averages calculated from the TIC data are compared to the upstream averages estimated from the AMTV data in Fig. 16. Only AMTV data from under the lead are plotted. Each AMTV data point represents the heat flux averaged over a 100-m block of sampling, placed at the center time of the sampling. There are four groups of AMTV data points, each group corresponding to 1 of the 4 runs on day 219. Each TIC data block also represents 100 m, determined using the sampling time and ice drift speed (e.g., a 100-m mast data point consists of an 11.1-min average of the heat flux since the mast is moving at 0.15 m s^{-1} relative to the water), and is also placed at the center time of the block. The average for the entire day is shown as a horizontal line for the AMTV (100 W m^{-2}) and TIC (138 W m^{-2}); and a vertical bar for each indicates plus or minus 1 sample standard deviation of the block averages (57 or 78 W m^{-2} , respectively). Although the sample points from the AMTV and TIC may represent the same time, the two instruments were not in the same location, except when the vehicle crossed the lead edge. Flux averages from the mast show an increase from 90 to 375 W m^{-2} during the 2 h around AMTV run 1, followed by a decrease to values between 50 and 150 W m^{-2} over the next 6 h. The AMTV data also show the largest values near the beginning of the series, with the heat flux diminishing later in the day.

The first two AMTV runs show lower fluxes than the TIC, except when the AMTV was near the lead edge. Indeed, the largest AMTV fluxes were encountered near the downstream edge of the lead. (Boxes around the AMTV data points indicate blocks centered less than 200 m from the ice edge.) For example, the AMTV point just before the start of day 220 in Fig. 16 corresponds to the event less than 100 m upstream of the lead edge in Fig. 15. We hypothesize that the large fluxes at the lead edge were a natural consequence of an accumulation of radiative heating in the downstream direction in the upper layers of the open lead. This would result in the surface water temperature and turbulent heat flux being a maximum near the downstream lead edge. Later in the day, a steady state appears to have been reached with the AMTV data overlaying the TIC data nicely.

Despite the much larger temperature and salinity fluctuations, the vertical water velocity is actually weaker and of a higher-wavenumber character than either LeadEx or ANZFLUX. The melting pack ice is a source of freshwater that has a significant stabilizing effect and counters the shear-driven turbulence. The character of the turbulence at SHEBA is expected to be different for this reason. The turbulence likely becomes more energetic under the ice partly because the reduction of a stabilizing buoyancy flux allows shear to generate more turbulent energy. The reduced buoyancy flux under the ice also results in a larger characteristic eddy size.

4. Summary

Kalman smoothing of underwater vehicle motion leads to accurate estimates of vertical water velocity deviations. We have shown this with a comparison to the proven turbulence instrument cluster. Both the ACTV and AMTV vertical water velocity spectra show good agreement with simultaneous turbulence frame measurements, especially when one considers the limitations of the variability of the turbulent environments where the comparisons have been made. The heat (salt) fluxes were calculated directly using the Kalman smoother-derived vertical water velocity and temperature (salinity) deviations. These average fluxes from the AUVs compare well to flux estimates from the TIC. Although the ANZFLUX vehicle data were not accompanied by simultaneous TIC data, the heat and salt flux estimates are reasonable in direction and magnitude when put in the context of the surface heat fluxes.

The scales at which an AUV can gather turbulence data are on the order of a few meters to several hundred meters, at least for the AMTV. In contrast, the towed vehicle of Fleury and Lueck (1994) uses a shear probe to measure turbulent fluxes directly on scales of 25 cm–1 m. The submarine measurements of Yamazaki and Osborn (1993) include direct flux measurements in the range from 3 cm to 30 m using a shear probe, however, the operational constraints and expense of a submarine

are severe drawbacks. The Kalman smoothing method can be applied to any AUV with commonplace sensors. The high-wavenumber limit of vertical water velocity estimation ultimately depends on the size of the vehicle and the sensitivity of the motion sensors.

Horizontal profiles of temperature, salinity, and vertical water velocity fluctuations are useful because they reveal the spatial variability of heat and salt flux under varied surface conditions. An AUV can take snapshots of horizontal variability at many depths without disturbing the surface. The Kalman smoothing technique greatly improves the utility of virtually any AUV because it measures turbulent vertical velocities at the energy-containing scales of ocean boundary layer turbulence. It does this with no sensors beyond the usual AUV guidance and control sensors. However, the best results are obtained when the highest quality sensors are used and pitch and pitch rate are measured in addition to depth. Perhaps the greatest benefit of the Kalman smoother method is that because it does not require comparison with fixed point measurements, it allows turbulence estimates that are robust to changing boundary layer conditions. We will use the Kalman smoothing method and the AMTV to provide essential insight to the surface heat budget calculation and under-ice boundary layer processes at SHEBA.

Acknowledgments. The authors would like to acknowledge the support of the Office of Naval Research (Grants N00014-96-1-5033 and N00014-98-1-0037) and the field support of the National Science Foundation Office of Polar Program's SHEBA project (OPP-9701831). Also thanks to Don Percival and Bradley Bell for acting as statistical consultants and Tim Peterson for his early advice. Special acknowledgments are given to Miles McPhee for providing instruments and data for all three experiments. Finally, we acknowledge Peter Guest for supplying the ANZFLUX meteorological data and Russ Light and David Morison for their critical roles in AMTV and TIC work during the SHEBA field experiment.

APPENDIX A

The Kalman Smoother

Kalman filtering and smoothing are algorithms that produce a minimum error estimate of the state of a system for which one has noisy measurements. We present the equations used for the Kalman smoother as described in Gelb, where a full derivation can be found (Gelb 1974, p. 156). On a terminology note, filtering means to estimate the state at the just-measured time using past data. Smoothing is to estimate the state using measurements before and after the time point of interest, maximizing the amount of information used.

The state estimated by the smoother is a linear combination of the states estimated by the forward and back-

ward filters. The forward filter equations are (4) and (5). The backward filter is similar to the forward filter except when solving the differential equations, one must integrate backward in time (see below). Obviously the backward filter can only be applied after all data has been collected from $t = 0$ to $t = T$. With forward- and backward-state estimates and error covariance matrices at each time step, an optimal smoother can be derived. The optimum linear combination of the forward and backward estimates is found by requiring that the smoother estimate is unbiased and that the smoother error covariance is minimized. The optimum smoother is given by the following equations (Gelb 1974, p. 158). The subscripts refer to smoothed, forward, and backward estimates, and the \mathbf{P} matrices are defined similarly to \mathbf{P}_f :

$$\mathbf{P}_s^{-1} = \mathbf{P}_f^{-1} + \mathbf{P}_b^{-1} \quad (A1)$$

$$\mathbf{x}_s = \mathbf{P}_s(\mathbf{P}_f^{-1}\mathbf{x}_f + \mathbf{P}_b^{-1}\mathbf{x}_b). \quad (A2)$$

To integrate the backward filter, we define a new time variable $\tau = T - t$, and integrate from $\tau = 0$ to T . A problem arises when specifying the initial conditions for the backward estimate because at the end of the observation interval ($\tau = 0$), we only have that the forward estimates of both \mathbf{x} and \mathbf{P} must be the same as the smoothed estimates. This implies $\mathbf{P}_b^{-1}(\tau = 0) = \mathbf{0}_{m \times m}$, where m is the length of the state vector. We do not have enough information to get an initial condition on \mathbf{x}_b , so we transform the backward filter by defining a new quantity, \mathbf{s} :

$$\mathbf{s} = \mathbf{P}_b^{-1}\mathbf{x}_b. \quad (A3)$$

Since $\mathbf{x}_b(\tau = 0)$ is finite, $\mathbf{s}(\tau = 0) = \mathbf{0}$. Transforming the backward filter leads to the following equations that are integrated from $\tau = 0$ to T (Gelb 1974, p. 160):

$$\frac{ds}{d\tau} = (\mathbf{F}^T - \mathbf{P}_b^{-1}\mathbf{G}\mathbf{Q}\mathbf{G}^T)\mathbf{s} + \mathbf{H}^T\mathbf{R}^{-1}\mathbf{z} \quad (A4)$$

$$s(\tau = 0) = \mathbf{0}_{m \times 1}$$

$$\frac{d\mathbf{P}_b^{-1}}{d\tau} = \mathbf{P}_b^{-1}\mathbf{F} + \mathbf{F}^T\mathbf{P}_b^{-1} - \mathbf{P}_b^{-1}\mathbf{G}\mathbf{Q}\mathbf{G}^T\mathbf{P}_b^{-1} + \mathbf{H}^T\mathbf{R}^{-1}\mathbf{H} \quad (A5)$$

$$\mathbf{P}_b^{-1}(\tau = 0) = \mathbf{0}_{m \times m}.$$

The optimal linear smoother is then the set of Eqs. [4), (5), (A1), (A2), (A4), (A5)]. The set of equations has been implemented in MATLAB in the continuous formulation. Once initial conditions and matrix values are set, an ODE solver is called every time step, utilizing new measurements and the just-estimated state vector. Code is available from the authors. Before calculating the smoothed estimates (A1) and (A2), one must reverse the time series of \mathbf{s} and \mathbf{P}_b^{-1} to convert them from functions of τ to functions of t . The smoother outputs time series for the complete state vector and for the error covariance matrix.

APPENDIX B

Hydrodynamic Model for an Autonomous Underwater Vehicle

a. Hydrodynamic forces and moments

To find the hydrodynamic coefficients in Eqs. (6) and (7), we rewrite the hydrodynamic force terms as the sum of the lift forces of all vehicle components (B1). Drag is not included because the component of the drag forces in the vertical direction is balanced by the propulsion system:

$$F_h = \sum_j \frac{\rho}{2} AV^2 C_{lj}(\alpha) \approx \frac{\rho}{2} AV^2 \sum_j C_{l\alpha_j} \alpha_j$$

$C_{lj}(\alpha)$ = dimensionless lift coefficient for vehicle component j

α_j = angle of attack of component j

$$C_{l\alpha_j} = \frac{\partial}{\partial \alpha} C_{lj}(\alpha). \quad (B1)$$

The dimensionless coefficients, C_{lj} , depend on Reynolds number, shape of the particular component, and most importantly angle of attack. For small angles of attack and with the other factors held constant, C_{lj} can be written as a power series in α_j , in which all but the linear term are neglected, as in Eq. (B1). The hydrodynamic moments can be expressed in a similar fashion:

TABLE B1. ACTV and AMTV lift and moment coefficients and distances of the center of pressure from the center of gravity. The source of each value is indicated.

	Lift coefficient $C_{l\alpha_j}$		Moment coefficient $C_{m\alpha_j}$		Center of pressure X_j (m)	
	ACTV	AMTV	ACTV	AMTV	ACTV	AMTV
Hull	0.5 ^a	0.343 ^c	1.01 ^a	1.48 ^c	0.226 ^c	0.081 ^c
Dive planes	0.8 ^b	1.92 ^c	0.372 ^d	0.909 ^d	0.764 ^d	0.773 ^d
Ring	1.2 ^b	—	0.615 ^d	—	0.843 ^c	—

^a Hoerner (1975).

^b Brosseau and Ulbrich (1971).

^c Bottaccini (1954).

^d Calculated using other entries in the table [Eq. (B16)].

^e Measured.

BEST AVAILABLE COPY

$$L_h = \sum_j \frac{\rho}{2} V^2 A L C_{lhj}(\alpha) \approx \frac{\rho}{2} V^2 A L \sum_j C_{maj} \alpha_j. \quad (B2)$$

Formulas for lift and moment coefficients (C_{la} and C_{ma}) for many shapes have been determined, so we can regard them as known for each component composing the vehicle. Next, the angle of attack of each vehicle component is written in terms of the velocity of that component relative to the water at its center of pressure. The ACTV components are the hull, a ring protector around the propeller, and the dive planes while the AMTV lacks the ring:

$$\alpha_{hull} = \tan\left(\frac{w_{rel}}{u_v}\right) \approx \frac{w - w_w + V\theta}{V} \quad (B3)$$

$$\alpha_{ring} \approx \frac{w - w_w + V\theta + X_{ring}q}{V} \quad (B4)$$

$$\alpha_{dp} \approx \left(\frac{w - w_w + V\theta + X_{dp}q}{V} + \delta_p \right). \quad (B5)$$

Substituting Eqs. (B1)–(B5) for the hydrodynamic terms in (6) and (7) and using (8) gives the following result:

$$\begin{aligned} Z_w &= -\frac{1}{2} \rho V A (C_{lhull} + C_{loring} + C_{lodp}) \\ Z_q &= -\frac{1}{2} \rho V A \\ &\quad \times \left(2 \frac{\text{vol}}{A} k_1 + X_{hull} C_{lhull} + X_{ring} C_{loring} + X_{dp} C_{lodp} \right) \\ M_w &= \frac{1}{2} \rho V A (L C_{mahu} - X_{ring} C_{loring} - X_{dp} C_{lodp}) \\ M_q &= -\frac{1}{2} \rho V A (X_{hull}^2 C_{lhull} + X_{ring}^2 C_{loring} + X_{dp}^2 C_{lodp}) \\ Z_{dp} &= -\frac{1}{2} \rho V^2 A C_{lodp} \\ M_{dp} &= -\frac{1}{2} \rho V^2 A L X_{dp} C_{lodp}. \end{aligned} \quad (B6)$$

Unlike the other components, the effect of the hull on Z_q and M_q has not been incorporated through the angle of attack, α , in Eq. (B3), following Bottaccini (1954, p. 51).

b. Coefficients for vehicle body

For a symmetrical torpedo body, several authors have reported numerical values or empirical curves for lift coefficients (Nahon 1996; Bottaccini 1954). A good starting point is Eq. (B7) from Nahon (1996), although the ACTV required a number almost twice as large:

$$C_{lhull} = \frac{2(k_2 - k_1)A}{\text{vol}^{2/3}}. \quad (B7)$$

Bottaccini (1954, 25–28) suggests the following for lift and moment coefficients:

$$\begin{aligned} C_{lhull} &= 0.005 \left(\frac{L}{d} \right)^2 + 0.96 \frac{\text{vol}}{AL} \\ &\quad + 5.71 \left| 0.835 - \frac{\text{vol}}{AL} \right| - 0.012\omega \end{aligned} \quad (B8)$$

$$C_{mahu} = 2 \frac{\text{vol}}{AL} (k_2 - k_1) - \frac{X_{hull} C_{lhull}}{L} \quad (B9)$$

$$X_{hull} = 0.78(L - X_B)(1 - 0.0111\omega). \quad (B10)$$

All symbols are defined in appendix C. The angle, ω , is the trailing-edge angle in degrees, formed by a vertical at the rear tip of the vehicle and a line joining the tip with the boundary of the tapered tail section. These equations are only to be used for a trailing-edge angle between 7° and 90°, a ratio of length to diameter between 5 and 13, and a prismatic coefficient ($\text{vol } A^{-1} L^{-1}$) between 0.7 and 0.95. Although valid for the AMTV, these requirements are not met by the ACTV, so the lift coefficient and moment coefficients for the vehicle body are obtained from Hoerner and Borst (1975, p. 19-6, their Fig. 8).

c. Coefficients for control surfaces

The lift coefficient for the dive planes is determined from Bottaccini (1954, pp. 17, 46):

$$C_{lodp} = \frac{S}{A_0} \left[1 - \left(\frac{d_T}{b} \right)^2 \right] \frac{2\pi A_R}{(A_R^2 + 4)^{0.5} + 2}. \quad (B11)$$

Again, the parameters are defined in appendix C. The distance from the origin to the center of pressure of the fins is X_{dp} . The center of pressure is located at the quarter-chord point (the point one-fourth of the way from the leading edge of the fins on the root chord), and the moment coefficient follows [Eq. (B12)]:

$$C_{modp} = \frac{X_{dp} C_{lodp}}{L}. \quad (B12)$$

The values for the lift coefficient of the ACTV control planes and the ring protector were obtained from a report on the predecessor vehicle prepared by Lockheed Missiles and Space Company (Brosseau and Ulbrich 1971). The distance from the origin to the center of pressure of the ring surrounding the ACTV propeller is measured. The moment coefficient for the ring is also determined with Eq. (B12). The numerical values for the ACTV and the AMTV are in Table B1.

d. Modification for a horizontal variation in water velocity over the vehicle length

The AMTV model is expanded by one dimension to include two separate vertical water velocities: one for

the back half of the vehicle, w_b , and one for the front half, w_f . The time-lag relationship between the 2 velocities is given in Eq. (19). Since the control surfaces are at the rear of the vehicle, the control surface angle of attack involves w_b instead of w_w in Eq. (B5). The hull angle of attack uses the average of the front and back water velocities in place of the single water velocity in Eq. (B3). We also include a pitching moment that acts on the hull due to a water velocity that could be different at the front and rear hull sections. This torque is due to the difference between the average water velocity acting on the center of gravity and the water velocities at the front and rear sections. The lift forces are centered at $\pm L/4$, and we assume a lift coefficient of unity. The new pitching moment and heave due to water velocity are Eqs. (B13)–(B14). The terms shown

are in addition to those in Eqs. (6)–(7) that are not related to vertical water velocity:

$$m_T \dot{w} = \frac{1}{2} \rho V A \left[C_{l\alpha\text{hull}} \frac{w_f + w_b}{2} + C_{l\alpha\text{dp}} w_b \right] + \text{others} \quad (\text{B13})$$

$$J_y \dot{q} = -\frac{1}{2} \rho V A \left[L C_{m\alpha\text{hull}} \frac{w_f + w_b}{2} + 2 \left(\frac{L}{4} \right) \frac{w_f - w_b}{2} - X_{dp} C_{l\alpha\text{dp}} w_b \right] + \text{others.} \quad (\text{B14})$$

Equations (11)–(13) change to reflect the new parameterization of vertical water velocity, as well as the PI control system:

$$\mathbf{x} = \begin{bmatrix} w_b \\ w_f \\ w \\ q \\ z \\ \theta \\ z_{\text{errint}} \\ \theta_{\text{errint}} \end{bmatrix} = \begin{bmatrix} \text{vertical water velocity—back section} \\ \text{vertical water velocity—front section} \\ \text{vertical vehicle velocity} \\ \text{pitch rate} \\ \text{vehicle depth} \\ \text{vehicle pitch} \\ \text{integrated depth error} \\ \text{integrated pitch error} \end{bmatrix} \quad (\text{B15})$$

$$\mathbf{F} = \begin{bmatrix} -\frac{1}{\tau} & \frac{1.58}{\tau} & 0 & 0 & 0 & 0 & 0 & 0 & 0 \\ 0 & 0 & 0 & 0 & 0 & 0 & 0 & 0 & 0 \\ \frac{Z_{w_b}}{m_T} & \frac{Z_{w_f}}{m_T} & \frac{Z_w}{m_T} & \frac{Z_q + (m_L - m_T)V}{m_T} & \frac{-K_{zp}K_{\theta p}Z_{dp}}{m_T} & \frac{VZ_w + K_{\theta p}Z_{dp}}{m_T} & \frac{K_{zi}K_{\theta p}Z_{dp}}{m_T} & \frac{-K_{\theta i}Z_{dp}}{m_T} \\ \frac{M_{w_b}}{J_y} & \frac{M_{w_f}}{J_y} & \frac{M_w}{J_y} & \frac{M_q}{J_y} & \frac{-K_{zp}K_{\theta p}M_{dp}}{J_y} & \frac{VM_w + K_{\theta p}M_{dp}}{J_y} & \frac{K_{zi}K_{\theta p}M_{dp}}{J_y} & \frac{-K_{\theta i}M_{dp}}{J_y} \\ 0 & 0 & 1 & 0 & 0 & 0 & 0 & 0 & 0 \\ 0 & 0 & 0 & 1 & 0 & 0 & 0 & 0 & 0 \\ 0 & 0 & 0 & 0 & -1 & 0 & 0 & 0 & 0 \\ 0 & 0 & 0 & 0 & K_{zp} & -1 & -K_{zi} & 0 \end{bmatrix} \quad (\text{B16})$$

$$\mathbf{D}_1 = \begin{bmatrix} 0 \\ 0 \\ \frac{(mg - B)}{m_T} \\ \frac{BX_{CB}}{J_y} \\ 0 \\ 0 \\ 0 \\ 0 \\ 0 \end{bmatrix} \quad \mathbf{D}_2 = z_{\text{goal}} \begin{bmatrix} 0 \\ 0 \\ K_{zp}K_{\theta p} \frac{Z_{dp}}{m_T} \\ K_{zp}K_{\theta p} \frac{M_{dp}}{J_y} \\ 0 \\ 0 \\ 1 \\ -K_{zp} \end{bmatrix} \quad \mathbf{G} = \mathbf{I}_8. \quad (\text{B17})$$

Four new coefficients are then defined based on Eqs. (B13)–(B14):

$$\begin{aligned} Z_{w_b} &= \frac{1}{2}\rho VA \left(\frac{C_{l_{\text{chull}}}}{2} + C_{l_{\text{adp}}} \right) & Z_{w_f} &= \frac{1}{2}\rho VA \left(\frac{C_{l_{\text{chull}}}}{2} \right) \\ M_{w_b} &= -\frac{1}{2}\rho VA \left(\frac{LC_{m_{\text{chull}}}}{2} - \frac{L}{4} - X_{\text{dp}} C_{l_{\text{adp}}} \right) \\ M_{w_f} &= -\frac{1}{2}\rho VA \left(\frac{LC_{m_{\text{chull}}}}{2} + \frac{L}{4} \right). \end{aligned} \quad (\text{B18})$$

APPENDIX C

List of Symbols

All quantities are in the mks system, and angles are in radians, unless otherwise noted. Short descriptions and sign conventions are presented.

A	= maximum cross-sectional area of vehicle
A_R	= aspect ratio of dive planes = b^2/S
b	= lateral span of planes
B	= total buoyancy of body; positive quantity
C_p	= specific heat of seawater at constant pressure
d	= maximum vehicle body diameter
dp	= angle of dive plane relative to body; positive means front edge up
d_T	= average diameter of the body portion intersected by fins
g	= gravitational constant
I_y	= moment of inertia for a cylinder of uniformly distributed mass = $mL^2/12$;
J_y	= apparent moment of inertia = $I_y(1 + k' \rho \text{vol}/m)$
k	= horizontal wavenumber, in cycles per meter (cpm)
k_1	= $\alpha_0/(2 - \alpha_0)$
k_2	= $\beta_0/(2 - \beta_0)$
k'	= $\frac{\beta_0 - \alpha_0}{\left(\frac{L^2 + d^2}{L^2 - d^2} \right) \left[2 - (\beta_0 - \alpha_0) \left(\frac{L^2 + d^2}{L^2 - d^2} \right) \right]}$
K_{zi}	= proportionality constant between dive plane command and integrated depth error; positive
K_{zp}	= proportionality constant between dive plane command and depth error; positive
$K_{\theta i}$	= proportionality constant between dive plane command and integrated pitch error; positive
$K_{\theta p}$	= proportionality constant between dive plane command and pitch error; positive
L	= body length
m	= mass of vehicle, including fluid in any flooded sections
m_L	= apparent longitudinal mass = $m + k_1 \rho \text{vol}$

m_T	= apparent transverse mass = $m + k_2 \rho \text{vol}$
q	= vehicle pitch rate; positive means nose moving up
S	= planform area of dive planes
S'	= salinity deviations; detrended absolute salinity in psu
T'	= temperature deviations; detrended absolute temperature
V	= speed of vehicle relative to water
vol	= geometric volume of vehicle
w	= vertical vehicle velocity; positive downward; in earth-centered frame
w_b	= vertical water velocity at back half of vehicle; in earth-centered frame
w_f	= vertical water velocity at front half of vehicle; in earth-centered frame
w_v	= vertical vehicle velocity; in vehicle-centered frame
$w_{v\text{rel}}$	= vertical vehicle velocity relative to water; in vehicle-centered frame
w_w	= vertical water velocity; in earth-centered frame
X_B	= location of center of buoyancy; distance behind nose of vehicle
X_{CB}	= location of center of buoyancy; distance forward of center of gravity (CG)
z	= depth of vehicle; positive downward; in earth-centered frame
z_v	= depth of vehicle; positive downward; in vehicle-centered frame
α_0	= $\frac{2d^2}{L^2 - d^2}$ $\times \left\{ \frac{L}{(L^2 - d^2)^{0.5}} \ln \left[\left(\frac{d}{L - (L^2 - d^2)^{0.5}} \right) - 1 \right] \right\}$
β_0	= $\frac{L^2}{L^2 - d^2}$ $\times \left\{ 1 - \frac{d^2}{L(L^2 - d^2)^{0.5}} \ln \left[\frac{d}{L - (L^2 - d^2)^{0.5}} \right] \right\}$
θ	= pitch of vehicle; positive means nose up
ρ	= mean seawater density
ω	= trailing-edge angle for vehicle tail section in degrees (zero deg for body with no tapered tail)

REFERENCES

Bartlett, M. C., and T. L. Schlachter, 1967: Fundamental principles of torpedo dynamics. U.S. Navy Mine Defense Laboratory Tech. Note 134, 97 pp.

Bottaccini, M. R., 1954: The stability coefficients of standard torpedoes. U.S. Naval Ordnance Test Station 909, NAVORD Rep. 3346, 94 pp.

Brosseau, J. A., and H. G. Ulbrich, 1971: Hydrodynamic analysis and test of the APL target vehicle. Lockheed Missiles and Space Company Rep. D244667, 45 pp.

Etkin, B., 1972: *Dynamics of Atmospheric Flight*. Wiley, 579 pp.

Fleury, M., and R. G. Lueck, 1994: Direct heat flux estimates using a towed vehicle. *J. Phys. Oceanogr.*, **24**, 801–818.

Gelb, A., Ed., 1974: *Applied Optimal Estimation*. The MIT Press, 374 pp.

Guest, R. S., 1998: Surface longwave radiation conditions in the eastern Weddell Sea during winter. *J. Geophys. Res.*, **103** (C13), 30 761–30 771.

Hoerner, S. F., and H. V. Borst, 1975: *Fluid-Dynamic Lift*. L. A. Hoerner, 502 pp.

Jenkins, G. M., and D. G. Watts, 1968: *Spectral Analysis and Its Applications*. Holden-Day, 525 pp.

LeadEx Group, 1993: The LeadEx Experiment. *Eos, Trans. Amer. Geophys. Union*, **74**, 393, 396–397.

Levine, E. R., and R. G. Lueck, 1999: Turbulence measurement from an autonomous underwater vehicle. *J. Atmos. Oceanic Technol.*, **16**, 1533–1544.

Lueck, R. G., and F. Wolk, 1999: An efficient method for determining the significance of covariance estimates. *J. Atmos. Oceanic Technol.*, **16**, 773–775.

McPhee, M. G., 1994: On the turbulent mixing length in the oceanic boundary layer. *J. Phys. Oceanogr.*, **24**, 2014–2031.

—, and T. P. Stanton, 1996: Turbulence in the statically unstable oceanic boundary layer under Arctic leads. *J. Geophys. Res.*, **101** (C3), 6409–6428.

—, and Coauthors, 1996: The Antarctic Zone Flux Experiment. *Bull. Amer. Meteor. Soc.*, **77**, 1221–1232.

Morison, J. H., and M. G. McPhee, 1998: Lead convection measured with an autonomous underwater vehicle. *J. Geophys. Res.*, **103** (C2), 3257–3281.

—, T. B. Curtin, and C. A. Paulson, 1992: The oceanography of winter leads. *J. Geophys. Res.*, **97** (C7), 11 199–11 218.

Moritz, R. E., and D. K. Perovich, Eds., 1996: Surface heat budget of the Arctic Ocean Science Plan. ARCSS/OAII Rep. 5, 64 pp. [Available from Polar Science Center, Applied Physics Lab, 1013 NE 40th St., Seattle, WA 98105.]

Nahon, M., 1996: A simplified dynamics model for autonomous underwater vehicles. *Proc. 1996 Symp. on Autonomous Underwater Vehicle Technology*, New York, NY, IEEE, 373–379.

Osborn, T. R., and C. S. Cox, 1972: Oceanic fine structure. *Geophys. Fluid Dyn.*, **3**, 321–345.

Percival, D. B., and A. T. Walden, 1993: *Spectral Analysis for Physical Applications: Multitaper and Conventional Univariate Techniques*. Cambridge University Press, 583 pp.

Ruffieux, D., P. O. G. Persson, C. W. Fairall, and D. E. Wolfe, 1995: Ice pack and lead surface energy budgets during LEADEX 1992. *J. Geophys. Rev.*, **100** (C3), 4593–4612.

Wettlaufer, J. S., M. Grae-Worster, and H. E. Huppert, 2000: Solidification of leads: Theory, experiment, and field observations. *J. Geophys. Res.*, **105** (C1), 1123–1134.

Yamazaki, H., and T. R. Osborn, 1993: Direct estimation of heat flux in a seasonal thermocline. *J. Phys. Oceanogr.*, **23**, 503–516.

BEST AVAILABLE COPY